Politecnico di Torino

Collegio di Ingegneria Meccanica, Aerospaziale, dell'Autoveicolo e della Produzione
Corso di laurea in Ingegneria Aerospaziale

Tesi di Laurea Magistrale

Design and characterization of a fast response temperature probe

Relatori
Prof. Gaetano Maria Di Cicca
Prof. Michele Iovieno
Prof. Marco Belan

Correlatore
Dott. Sergio Lavagnoli

Candidato
Mattia Bassignana

Marzo, 2018

To my mother,
for her affection

Acknowledgments

First of all I need to thank my family, nothing would have been achievable without their support. Thanks to my mother for her great energy, her encouragements in achieving my objectives, her constant assistance also in quotidian things; thanks to my father for his wise advices and his silent but constant support.

A special thanks goes to Dr. Sergio Lavagnoli, my supervisor at VKI. I really appreciated his great example in hard working, his constant presence and great support, his ability in enhancing my qualities, his advices about work and life. Thank you also to Bogdan for his availability and help, especially during the last experimental part of my work at VKI. Thank you to my Italian supervisors: Prof. Di Cicca, Prof. Iovieno and Prof. Belan for the great opportunity they gave me to work in the exciting VKI environment.

Thanks to all my friend at the Crocetta University College. Especially my gratitude goes to Rodrigo, Luca, Gabriele and Jean for making amazing my five years stay in Turin; to Nicolò for the good time I spent with him and to Marc and Marco to be my mates during the hard working periods.

Thanks to Stefano for his important support during my last year at the Politecnico. A particular thanksgiving to Flavia and Laura for their friendship and support also from long distance.

I am also grateful to Marco and Pier for their reliable presence and for the excellent recreation opportunities they gave me.

Finally I need to mention my peers at VKI: Marco, Tamara, Nicolò and especially Matteo for his companionship during my life in Brussels.

Abstract

The performances of thermal engines are strictly related to the maximum temperature reachable at the combustion end. With a unique cold ring transient facility, it is possible to test at VKI a high pressure stage engine turbine in real Reynolds and Mach conditions. In this application the blade passing frequency is in the order of 7KHz so, for the accurate time resolution of the thermal field, it is required a measurement technique able to reach a frequency response of 25KHz or more. In order to reach this strict requirement the thin film technology is selected and a probe able to estimate the temperature from heat flux measurements is developed. The working principle consists in measuring probe wall temperature time histories in different thermal conditions, calculating the heat flux with a simplified model and through the heat flux vs temperature linearity, estimating the flow total temperature.
This probe needs to operate in transient mode with high spatial resolution (1mm); the classical double thin film approach [7], [23], [6], [35] is avoided. An innovative single thin film temperature probe is developed. Only one thin film sensor, crossed by constant current, is placed at each measurement point. The different thermal conditions, on the probe surface, are reached using a multi tests approach in the same flow conditions. A heater is placed inside the probe and during each test it warms the probe wall at different levels. With this technique, a more accurate best fit, instead of two points simple interpolation, is used.
With this work the probe is simulated on the aerodynamic and thermal point of view in order to investigate about: the probe measurement error and intrusiveness, the linearity of the heat transfer phenomena, the expected thermal field inside the probe and the efficiency of different post process algorithms. Finally, a probe prototype is built and tested in a jet able to reproduce the transient facility conditions. The main goals in the last part are: obtaining a stable calibration law for the thin film probe, detecting the linearity in the heat transfer phenomena and to evaluating the capability of the probe in the constant jet temperature measurements.

Italian Summary

Le prestazioni di un motore termico sono strettamente correlate alla massima temperatura del fluido in uscita dalla camera di combustione. Al Von Karman Institute, è presente un apparato molto particolare in grado di simulare, in termini di numero di Reynolds e di Mach, le condizioni presenti in uno stadio di alta pressione della turbina di un moderno motore aeronautico. In una applicazione di questo tipo la frequenza di passaggio delle pale è nell'ordine dei 7KHz. Per una accurata risoluzione temporale del campo termico è necessaria una tecnica di misura in grado di raggiungere una risposta in frequenza di almeno 25KHz. Per poter raggiungere questo requisito molto stringete è stata selezionata la tecnologia a thin film; una sonda in grado di stimare la temperatura totale del flusso a partire da misure di heat flux è stata concepita. L'idea di base consiste nella misura nel tempo della temperatura di parete della sonda in differenti condizioni termiche; utilizzando queste storie temporali è possibile calcolare, utilizzando un modello 1D semplificato lo scambio termico a parete. Quando le storie temporali di temperatura e scambio termico a parete, in diverse condizioni di riscaldamento della sonda, sono note, sfruttando la linearità del fenomeno convettivo, la temperatura totale del flusso può essere ottenuta.
La sonda in questione dovrà operare in condizioni di tipo transitorio mantenendo però una buona risoluzione spaziale (nell'ordine di 1 mm); per questo motivo l'approccio classico a doppio thin film per ogni punto di misura ([7], [23], [6], [35]) viene in questo caso scartato. Per l'applicazione in questione è stata sviluppata una sonda innovativa a singolo thin film. In ogni punto di misura viene inserito un solo thin film alimentato con corrente costante. Le diverse condizioni termiche sulla superficie della sonda sono ottenute sfruttando un approccio multi test. Un heater è inserito all'interno della sonda e più test sono ripetuti nelle stesse condizioni di flusso andando a riscaldare la sonda a differenti livelli. Sfruttando questa tecnica la linearizzazione, temperatura di parete vs scambio termico a parte, può essere effettuata su più punti tramite il metodo dei minimi quadrati, al posto che con semplice, e meno accurata, interpolazione lineare su due punti. Un altro grande vantaggio consiste nell'evitare la presenza di due thin film a differente temperatura molto vicini tra loro. Questi potrebbero generare gradienti termici e quindi flussi di calore laterali impossibili da considerare con un modello semplice monodimensionale. In applicazioni a funzionamento transitorio sarebbe inoltre molto difficile mantenere apprezzabile la differenza di temperatura tra i thin film durante il test. Questo a causa della grande differenza di condizione convettiva tra la fase pre-test

e la effettiva fase di misura. Il grande svantaggio in questo approccio a singolo thin film è la necessità di più test per ogni punto di misura. Differenti criticità legate alla ripetibilità dei test e alla sincronizzazione dei segnali provenienti dalle varie prove vengono in questo caso introdotte.
Questo lavoro vuole occuparsi in un primo momento della simulazione del campo aero termico presente attorno alla sonda. Diverse simulazioni sono state lanciate per ottenere la distribuzione di temperatura di recupero e numero di Nusselt sulla superficie della sonda. Altre simulazioni CFD sono state utilizzate per potere validare la linearità del fenomeno convettivo nel range operativo di temperature previsto per la sonda. Infine uno studio volto a indagare i deboli effetti non lineari nel fenomeno è stato sviluppato, ottenendo risultati coerenti con la letteratura [19].
In una seconda parte partendo da alcune considerazioni analitiche una prima geometria per la sonda è stata proposta. Utilizzando un approccio agli elementi finiti il campo termico, non stazionario interno alla sonda durante i test è stato simulato con modelli bi e tri dimensionali. I risultati numerici sono stati anche utilizzati per sviluppare e testare due diversi metodi di post processing. Infine un procedura utile a progettare il sensore thin film andando a massimizzare segnale di output e rapporto segnale rumore è stata implementata e utilizzata per il caso in questione.
Nell'ultima parte di questo lavoro, sfruttando il prototipo costruito dal tecnico del VKI, alcuni test preliminari con la sonda sono stati effettuati. In un primo momento è stato necessario assicurare la stabilità nella legge di calibrazione del sensore. Successivamente le condizioni transitorie, di Reynolds e di Mach sono state riprodotte con un getto riscaldato. Sfruttando questo lavoro sono state svolte prove utili a valutare: la riproducibilità del flusso, la linearità del fenomeno convettivo e la capacità della sonda di misurare correttamente la temperatura del getto.

Contents

List of Figures

List of Tables

List of Symbols

Acronyms

FEM	Finite elements
FT	Fourier transform
RANS	Reynolds average Navier Stokes equations
TP	Thermal product
TU	Turbulence intensity
VKI	von Karman Institute

Roman symbols

Re	Reynolds number	-
Nu	Nusselt number	-
St	Strouhal number	-
c_p	pressure coefficient	-
c_l	lift coefficient	-
c_d	drag coefficient	-
c_p	constant pressure heat flux	$J/(KgK)$
c_p	constant density heat flux	$J/(KgK)$
k	thermal conductivity	$W/(mK)$
f	frequency	Hz
h	heat transfer coefficient	$W/(m^2K)$
p	pressure	Pa
q	heat flux	W/m^2
r	radial coordinate	m
T	temperature	K
u	x- (axial) component of velocity	m/s
v	y- (radial) component of velocity	m/s
V	velocity	m/s

Greek symbols

γ	c_p/c_v	-
δ	boundary layer thickness	m
ρ	density	kg/m^3
ϕ	phase	

Sub- and Superscripts

a	adiabatic
amb	value relative to the ambient
$cond$	conductive
$conv$	convective
d	dynamic
eff	effective
fl	value relative to the flow
o	total
w	value referred to the wall

Introduction

The last 20 years have seen a dramatic increase of air traffic, leading to a renewed interest in the studies aimed to improve aircraft efficiency in order to reduce flight times, costs, pollution and noise. The main goal of turbomachinery research is to increase engine energy efficiency, performances, reliability and maintainability and reducing weight, noise and pollution emissions. This thesis has been carried out at the VKI TU department, which is very active in these fields and has brought many contributions with its numerical and experimental studies to increase the scientific and technical knowledge in this field.
Ideally, an aircraft engine could be thermodynamically modelled with a Joule-Brayton cycle. In the ideal case the Joule Brayton efficiency depends only on the compressor pressure ratio β

$$\eta = 1 - \frac{1}{\beta^{\frac{\gamma-1}{\gamma}}} \tag{1}$$

The resulting work per mass unit is related to the maximum temperature T_3 reached at the turbine entrance.

$$\frac{L}{c_p T_1} = \frac{T_3}{T_1}\left(1 - \frac{1}{\beta^{\frac{\gamma-1}{\gamma}}}\right) - \left(1 - \beta^{\frac{\gamma-1}{\gamma}}\right) \tag{2}$$

On the other hand, the real case presents losses due to flow irreversibility, not isoentropic compression and expansion and secondary flows. In this case also the cycle efficiency is influenced by the engine temperature ratio T_3/T_1. Figure 1 shows, qualitatively, the cycle work and efficiency, by varying the temperature ratio. In the real case, increasing the temperature ratio leads to positive consequences to both the work and the cycle efficiency. T_1 is fixed by the flight conditions, so the simplest method to increase the engine temperature ratio is raising T_3.

Thermal and fluid dynamics turbine field characterization

The high pressure turbine stage is located just downstream the combustor. In this position the operating conditions are very severe in terms of aerodynamics, mechanical and thermal loads. Actually the main limit in increasing T_3 comes from the thermal and

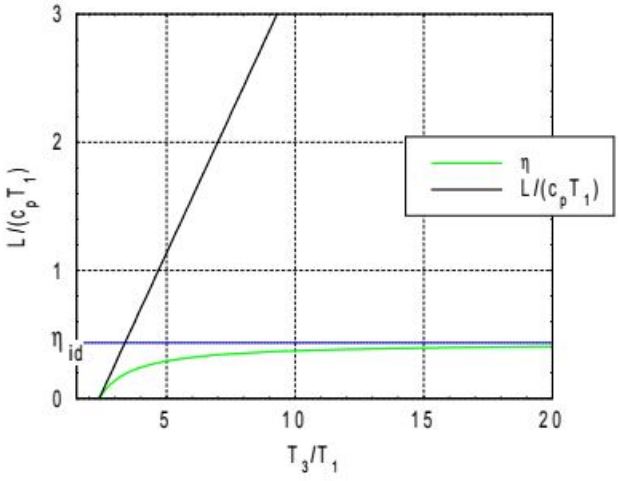

Figure 1: Work and efficiency of Joule Braiton cycle

mechanical resistance of the first high pressure stage. Different kinds of cooling systems have been developed in order to preserve the first stage turbine blades. Furthermore, in this region also temperature fluctuations can be relevant, due to the periodic blade passage, combustor unsteadiness and turbine secondary flows. In order to improve the turbine design, reducing losses and increasing performances, it is very interesting to estimate these fluctuations and to characterize the turbine stage temperature field. In this region the fluid dynamics field is ruled by the periodic blade passage. The turbine rotation speed, in a modern aircraft is in the order of some thousands of RPM; considering 100 blade mounted on the rotor the blade passing frequency for a modern aircraft turbine is in the order of some kHz. This reason justifies the request of high time resolution for the fluid dynamics characterization; typically 10 or more kHz are required.
Some numerical analysis are carried out. Shyam V. et all [34] simulated a stage of modern high pressure turbine using a RANS technique and setting 50 time steps for each blade passage. Green B. R. [13] studied a high pressure turbine stage and compared the results coming from numerical and experimental analysis. In this case they solved the numerical problem setting 72 time steps for each blade passage but, they were able to evaluate experimentally, with this very high time resolution, only the pressure field behind the turbine stage. It is very difficult to measure temperature fluctuations with time resolution able to keep up with the blade passing frequency. With the classical measurement techniques (thermocouples or cold wires) it is impossible to reach this very high frequency response (more then 10 kHz). This is why new concept temperature probes are required. Some preliminary attempts have been carried out in this direction. Mansour et all [23] measured the entropy fluctuations behind a centrifugal compressor stage with a probe built using a high response pressure sensor coupled with a temperature double thin film system. Buttsworth et al [6] measured the temperature fluctuations behind a turbine stage using a double prong thin film probe. Arenz et al.[1] developed a single

thin film temperature probe and used it to characterize the thermal field behind a low pressure, two stage turbine test ring.

Thesis goals

A high response temperature probe is required to carry out unsteady temperature measurement in the CT3 (dynamics isoentropic compression tube) of von Karman Institute for Fluid Dynamics. This facility is able to simulate in terms of Reynolds and Mach number, the usual conditions of a modern aircraft engine high pressure turbine stage.
With this work we developed a new concept heated, single thin film, probe. Our first purpose was to implement numerical models able to simulate the probe, in its operating conditions, on the fluid dynamics and thermal point of view. Using the simulations results a preliminary design was carried out.
In a second time we estimated the error, made by the probe, in the total temperature measurement. Using the fluid dynamics simulations it is possible to understand how the probe-flow misalignment and the probe intrusiveness can influence the temperature measurement. We developed and tested numerically a post process algorithm in order to understand the probe error in the total temperature reconstruction.
Finally, the VKI technician built the first probe prototype with which we carried out some preliminary experimental tests in controlled flows. The final goals, in this step, are to validate the numerical calculations, test the post process routine and estimate the probe error in the total flow temperature measurement.

Thesis outline

Chapter 1 introduces some examples of thin film probes. Most of all, we analysed the probes developed in Zurich ETH, Stuttgard and Oxford are analysed. Starting from a general description of VKI CT3 facility some design requirements are fixed. In the end the general working principle is described.
Chapter 2 contains the fluid dynamics analysis. The chapter starts with some analytical and experimental results coming from literature. The following part contains the CFD analysis useful to estimate the error caused by the flow misalignment and by the probe intrusiveness. The end of this chapter presents a study useful to understand the heat flux phenomena and its non linearities. All the fluid dynamics analysis are made at different turbulence levels
Chapter 3 includes the probe heat conduction analysis. A 2D model is built and CT3 flow conditions are simulated. The post process algorithm is developed and tested on the numerical data. Finally, we built and computed a 3D model able to estimate also the 3D conduction effects. In the end of the chapter we used the same kind of analysis to simulate a probe built with different double layer technique.
Chapter 4 reports all the experimental tests and analysis. The CT3 conditions are reproduced with a open jet, the probe and the post process procedures are tested.

Chapter 5 contains the concluding considerations.
Chapter 6 contains the future possibles developments of this work.

Chapter 1

Thin film probes

Different techniques are developed to measure the temperature in flows. The simplest one, takes advantage from a particular thermoelectric effect, which allows to measure a voltage difference in a electric circuit made by two different conductors, when a temperature gradient is present; thermocouples sensors use this principle. Another type of thermal sensors are the cold wire probes. With this technique a thin wire is positioned in the flow, the wire is traversed by electrical current and heated by the flow. The wire resistance depends on the wire temperature. It is possible, measuring the current and the tension difference on the wire, to estimate the flow temperature. These techniques are well known, tested and defined. The problem is that, due to materials thermal inertia, the maximum temperature fluctuation detectable with the cold wire technique is around 1 kHz. Worse performances are reached with the thermocouples. As explained in the first chapter this dynamic response is not enough for turbomachinery applications. One possible solution is given by thin film probes. These are a very innovative kind of temperature probes theoretically able to reach frequency response in the order of 50 kHz or more. The basic principle is to measure the probe wall temperatures and wall heat fluxes, heating the wall at different levels. With a linear interpolation it is possible to reconstruct the probe adiabatic wall temperature that, at the stagnation point, coincide with the flow total temperature. Basically, with the heat flux measurement at different wall temperatures it is possible to estimate the flow temperature. The heat flux measurements are carried out using very thin resistance sensors (their thickness is in the order of 100nm or less) called thin films.

1.1 Oxford double thin film probes

In the Oxford university Department of Engineering Science two different kind of double thin films probes are developed. The first one [6] is built with two quartz prongs (figure 1.1). On each prong extremity a platinum thin film is painted. A heating element, made by a electrical resistance, is placed into the upper prong. Switching on the heater, it is possible to reach, between the prongs, a temperature difference of almost 50 K. Placing the probe in the unknown flow, with the heater switched on, it is possible to measure

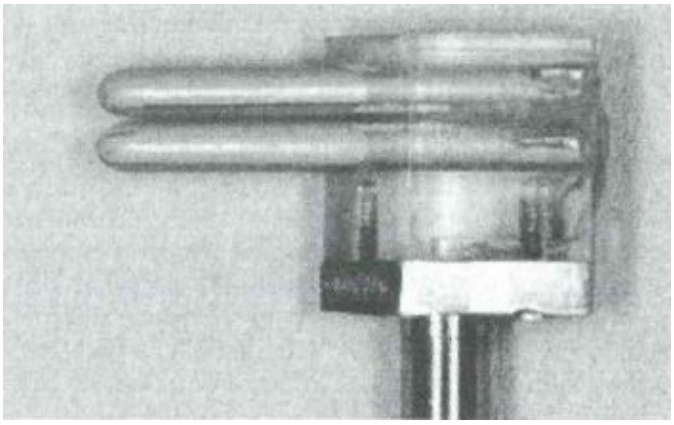

Figure 1.1: Oxford double prongs probe

two different heat fluxes time histories at different wall temperatures. This probe is used in transient facilities so, during the experiments, it is instantaneously placed in a hot flow for 600 ms and the two wall temperature time histories are measured. Starting form the wall temperatures, with a 1D algorithm, the total wall heat flux is computed. By knowing the electrical current and the potential different on the thin films it is possible to estimate the convective heat flux:

$$q_{conv} = q_{tot} - I\Delta V \tag{1.1}$$

With this method it is possible to know the wall temperature and the heat flux time histories in two different heating conditions. Using this informations, with a linear interpolation, the adiabatic wall temperature is evaluated:

$$T_{aw} = T_{w1} + q_1 \frac{T_{w1} - T_{w2}}{q_1 - q_2} \tag{1.2}$$

In the same department another high response temperature probe is developed[6]. The final goal, in this case, is the increase of spatial resolution. Two thin films are placed on top of a single, quartz, 2.8 mm diameter prong with a distance of 0.7mm (figure 1.2). It is required to reach two different wall temperatures so the two thin film have different resistance (44 and 58 Ω). In order to maintain the temperature difference even during the test, when the convection effects are very strong, the two resistances are crossed with different current intensities (15 mA and 70 mA). Here, the problem comes before the test beginning: the convection on the probe is very low and the high current on the hot thin film can generate excessive wall temperatures that can influence the temperature on the cold thin film . For this reason, on the hot thin film the high current level, is switched on only 1 s before the test begins.

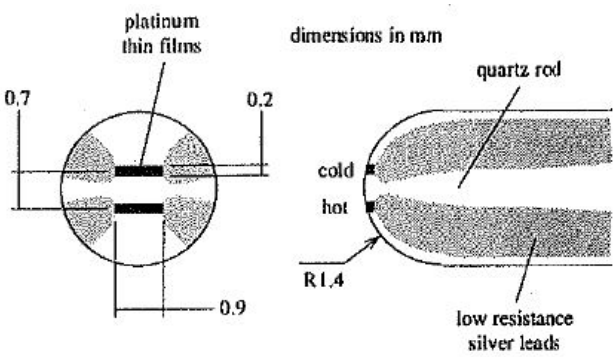

Figure 1.2: Oxford single prong probe

1.2 Zurich high response entropy probe

The third example of thin film probe comes from the Turbomachinery laboratory of ETH university in Zurich[22]. They developed an unsteady entropy probe able to evaluate the entropy fluctuations in the "Rigi" test facility that can simulate a centrifugal compressor stage. In this case the facility is working in continuous mode, so the probe has to work for a long time in thermal equilibrium with the flow. For the unsteady entropy measurement, a high response temperature and high response pressure sensors are coupled. The entropy is evaluated as:

$$\Delta s = c_p ln \frac{T}{T_{ref}} - Rln \frac{p}{p_{ref}} \tag{1.3}$$

Figure 1.3 shows the complete probe with the two sensors. The unsteady temperature

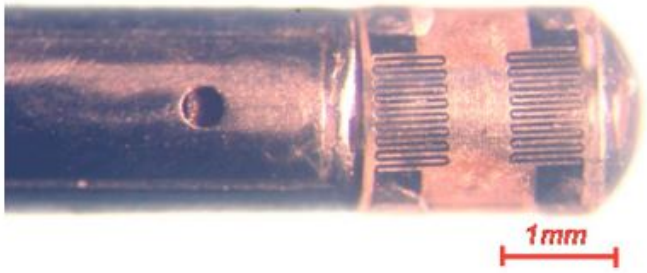

Figure 1.3: Zurich high response entropy probe

sensor is made using two thin film deposed on a the 1.8mm diameter cylindrical quartz substrate. The working principle is the same adopted at Oxford university. At different heat flux conditions the wall temperatures are measured. With a 1D algorithm the wall heat flux is estimated and finally, with a linear interpolation, also the adiabatic wall temperature, equal at the stagnation point to the flow total temperature, is computed. In this case the probe is operating in continuous conditions, so during the test the probe

substrate is in thermal equilibrium with the flow. The two different wall temperatures are reached by providing different electrical currents to the thin films.

1.3 Stuttgard high response temperature probe

Even in this case a high response temperature probe, able to measure the temperature fluctuations in a turbine test ring is required[1], the idea is similar: measuring wall temperatures in different heat flux conditions, estimating the convective heat flux and, with linear interpolation, calculating the adiabatic wall temperature. The probe is built with a 1 mm diameter quartz cylinder. The 125 nm thick platinum thin film is manufactured on a polyimide layer of 20 μm, later glued on the probe substrate. In this case the post process algorithm is more elaborate; to obtain the wall heat flux it is necessary to include, in the conduction model, the effect of three materials: the polyimide layer, the glue and the quartz substrate. On this probe only one thin film is mounted; the advantages are the spatial resolution increase and the solution of all interference problems between the thin films. On the other hand, at least two tests run at the same flow conditions are required to evaluate the adiabatic wall temperature evaluation. At each measurement point the thin film is consecutively operated at two different constant currents, and therefore, at two different overheat wall temperatures. The voltage drop across the sensor element is measured; moreover the wall temperature is deduced from the calibration law. The heat flux time history is obtained using a 1D model. Finally, using linear interpolation, the adiabatic wall temperature is computed.

1.4 Design requirements

At VKI some studies on thin film temperature probes were developed in the past. For istance a double prong probe similar to the Oxford one was manufactured [35]. Some preliminary studies on a double thin film probe were also carried by A. J. Carvalho [7]. Starting from these preliminary experiences, we want to develop a high response temperature probe able to measure temperature fluctuations in the VKI CT3 test ring. This facility is able to reproduce, in terms of Mach and Reynolds number, the flow existing in a modern aircraft engine high pressure stage turbine. The CT3 is a blow down test ring built with three main components: the compression tube, the test section and the dump tank (figure 1.4). The test section is separated from the compression tube with a fast response shutter valve. Downstream the test section, an adjustable sonic throat is positioned. Regulating the sonic throat area, the exiting flow ratio is maintained equal to the entering one in the test section. In a typical test, the shutter valve is initially closed and in the upstream tank the piston is in the back of the cylinder, the pressure is regulated and the temperature is equal to the ambient one. In the dump tank, starting from ambient conditions, the vacuum pumps create a low pressure conditions (p=25mBar absolute pressure).Meantime the lubrication system is switched on and the rotor is put in rotation. Then, pressurized air coming from high pressure reserve (300 bar) is regulated and expanded at the back of the cylinder. The piston

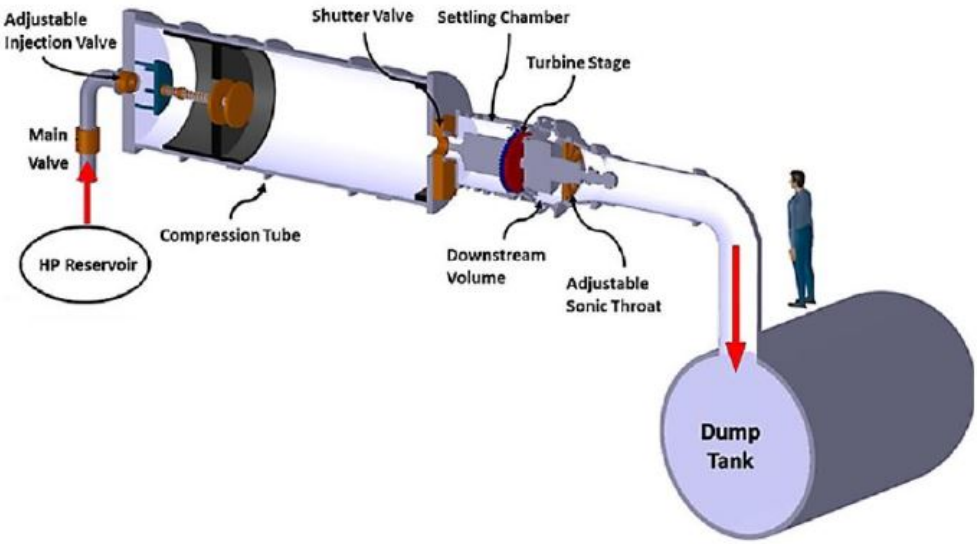

Figure 1.4: General schema of CT3 facility

starts to slide and a quasi isoentropic compression in the compression tube is performed. When the pressure reaches a specific value the shutter valve opens and the pressurized hot air is discharged in the test section. The final goal of this work is to produce

Figure 1.5: External view of CT3 facility

a probe able to measure temperature fluctuations during the 0.7 s test in CT3. The probe has to resolve the temperature variations associated at the blade passing, so the required frequency response has to be very high. (in the order of 25kHz). The spatial resolution is imposed by the tip clearance (less than 1mm). Downstream the rotor the flow is highly three-dimensional and the fluctuation in velocity and yaw angle could be very large. The probe has to present very low sensibility to the attack angle between

Figure 1.6: Rotor of CT3 anular cascade test section

+40 and -40 deg. The final probe has to work with temperature ranging from 300 to 380 K in a Mach range between 0.1 and 0.4. A good accuracy in the temperature estimation is required: ideally the error is in the order of 1K. Other important points are to reduce the probe blockage effect, to control the intrusiveness, studying and limiting the temperature fluctuations introduced by the probe. Finally, easy manufacturability, low costs and simple measurement procedures are appreciated features for the probe.

1.5 Working principle and general probe configuration

Due to the strict requirements in terms of frequency response the thin film technology is selected for the probe. The selected approach considers a single thin film sensor. With this choice, the spatial resolution is maximized and at the same time all problems regarding the presence of two close thin film, with different temperature, in transient heat flux condition are solved. The Oxford approach, with instantaneous high current on one thin film is avoided because the step in the electrical heat flux could influence the substrate thermal field and introduce errors in the heat flux estimation. In our case the different wall temperatures between different tests are not obtained with different currents on the thin film (Stuttgard approach). A heater is inserted inside the probe substrate. Through this, it is possible to warm up the probe and reach different wall temperature, keeping the thin film current constant and equal to the design current, able to maximise the sensibility and reduce the noise. With this solutions it is also easy to carry out, in the same flow conditions, measurements at more than two different wall temperatures. With these temperatures, it is possible to reduce the error in the total temperature measurement using a best fit algorithm instead of a simple linear interpolation. Figure 1.7 illustrates a qualitative example of this. Starting from a first estimation of the adiabatic wall temperature, regulating the heater power, it is possible to measure the heat flux at wall temperatures close enough to the flow adiabatic wall

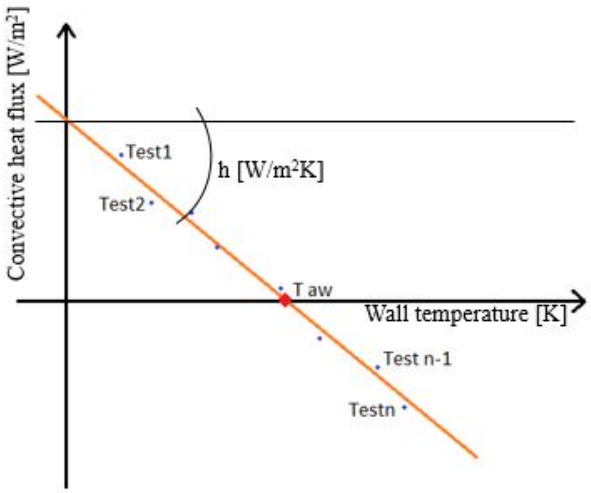

Figure 1.7: Example adiabatic wall temperature best fit interpolation

ones. In this way, even an error in the slope coefficient h, has little influence on the total temperature measure. In order to limit the number of tests required to cover all the blade span additional thin film are mounted on the probe height. Their number has to be defined in order to select a mutual distance able to avoid their mutual interference. The sensors numbers is also limited by the possibility to manufacture the electrical connections.
Summarizing, during the test the thin films will be crossed by constant current, the potential difference will be measured it will be possible to calculate the wall temperatures using the thin film calibration laws. Starting from the wall temperature, with a new corrected 1D algorithm, the local wall heat flux is computed. In the end using the wall temperatures and heat fluxes at different probe thermal conditions the adiabatic wall temperature is obtained.

Chapter 2

Fluid dynamic behaviour

This chapter discusses about the temperature probe, fluid dynamics behaviour. Finally the probe will be a cylinder with a length/diameter ratio higher than 10. For the fluid dynamics simulations the probe is modelled as a 2D cylinder. The advantage of the 2D case is the possibility to obtain accurate simulations limiting the computational cost. In literature it is easy to find studies about flow around cylinders, therefore it is not difficult to find experimental and numerical data for the model validation. The final goal of this study, is to obtain the adiabatic wall temperature distribution around the cylinder in terms of mean value and fluctuations. With these data is possible to estimate the error, made by the probe, in the total temperature measurement. The first approach is based on some analytical results coming form literature. In a second time a numerical, 2D model is developed and solved using the software Anys Fluent. In literature it is easy to find results about pressure distribution around cylinders, more difficult is to find data about the wall temperature. We validated the computed pressure field with data coming from literature; later using the same model we calculated the wall temperature distribution is obtained. In a second time, other numerical simulations are launched in order to estimate the local convective heat flux coefficient, the local Nusselt number and the non linear effects in the convective heat flux phenomena. We repeated these studies for two different levels of inlet turbulence, in order to understand also the role of this parameter in the convection phenomena.

2.1 Far field characterization

The first important point is to define the far field conditions, where the probe will be able to operate. The final goal is the flow temperature characterization in the VKI CT3 facility. The probe has to work, behind the stage rotor (plane 3), at different radios fig2.1 [3]. We consider also the possibility of an additional stator behind the rotor. The probe needs to work also in this new condition. The flow proprieties in this position are defined supposing a isoentropic expansion across the second stator; the final Mach number is fixed at 0.8 and all the flow proprieties are computed starting from the plane 3 conditions. Table 2.1 summarizes the flow proprieties in the most relevant CT3 positions.

	Plane 3			Plane 4
	Min	Max	Mean	Mean
T^o [K]	315	415	365	365
P^o [Pa]	42000	50000	46000	46000
T [K]	314	395	359	324
ρ $[kg/m^3]$	0.461	0.371	0.421	0.325
Mach	0.13	0.50	0.29	0.80
V [m/s]	44.8	200.5	109.8	288.46
Re/L [1/m]	$1.1 \cdot 10^6$	$3.3 \cdot 10^6$	$2.2 \cdot 10^6$	$4.8 \cdot 10^6$

Table 2.1: flow conditions

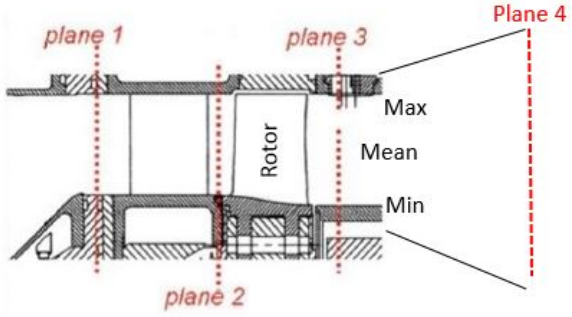

Figure 2.1: Facility scheme

2.2 Flow configuration around cylinders

In the last years a lot of experimental and numerical studies are carried out for the flow around cylinders characterization. The general arrangement of fluid dynamics field is strongly dependent from the Reynolds number. Table synthesizes the flow phenomenology by varying the Reynolds number 2.2. [20] For very low Reynolds numbers the viscous effects dominates, this case is called viscous regime and the flow remains completely attached at the cylinder surface. When the Reynolds increases two against rotating vortexes appear in the posterior part. For Reynolds numbers included between 40 and 150 the flow shows a very regular wake; in this case the vortex shedding is very regular and the associated frequency well defined. When the Reynolds increases again the cylinder enters in the transitional field; in this case the vortex shedding is not so regular. For higher Re number the wake became completely turbulent; the boundary layer in the forward part of the cylinder is still laminar, but at α around 80 deg the separation occurs and the wake is strongly turbulent. The last changing in the field phenomenology occurs

Reynolds range	flow type
$Re < 5$	Viscous flow
$5 < Re < 40$	fixed pair against rotating vortex
$40 < Re < 150$	laminar vortex street
$150 < Re < 300$	transitional vortex street
$300 < Re < 3 \cdot 10^5$	laminar separation turbulent vortex street
$Re > 3 \cdot 10^5$	turbulent boundary layer separation

Table 2.2: Flow arrangement

at $Re = 3 \cdot 10^5$, when the laminar boundary layer present the transition to turbulence. The boundary layer transition defers the separation and the separation point move in the posterior part of the cylinder. Due to this phenomenology the wake dimension and the drag coefficient are decreasing. In the nominal case (6 mm probe positioned in the plane 3 at middle radius) the expected flow configuration is characterized by turbulent wake with laminar boundary layer separation. Figure 2.2 represents this flow arrangement. In this configuration the vortex shedding dominates the fluid dynamics phenomenology.

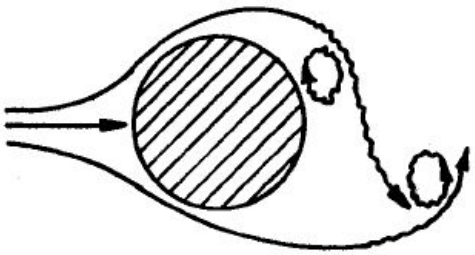

Figure 2.2: Flow configuration $Re = 1.3 \cdot 10^4$

It exists some empirical relations useful to estimate the typical frequency of this vortex periodic release. It is necessary to introduce the non dimensional frequency (Strouhal number).

$$St = \frac{f \cdot D}{V} \tag{2.1}$$

In our Reynolds range the correlation proposed by U. Fey et al[10] is very appropriate. They propose:

$$St = St^* + \frac{m}{\sqrt{Re}} \tag{2.2}$$

The selected nominal diameter for the probe is 6 mm. This is a typical diameter for this kind of application [7]. This diameter is enough for the sensor positioning, avoiding the thin film breakage; at the same time for greater diameters the probe intrusiveness grows too much. Another parameter, important to take into account in the probe diameter selection, is the shedding frequency. It is important to have a shedding frequency as

	Plane 3			Plane 4
	Min	Max	Mean	Mean
Re	$6.5 \cdot 10^3$	$2.0 \cdot 10^4$	$1.3 \cdot 10^4$	$2.9 \cdot 10^4$
St	0.21	0.19	0.20	0.19
f shedding [Hz]	1531	6457	3601	9163

Table 2.3: Shedding frequencies

much different as possible from the facility flow frequencies (blade passing frequency). For the selected diameter it is possible to calculate the Re number in each probe position; using the the equation 2.2 we are able to estimate the St number and the vortex shedding frequency.(table 2.3) Figure 2.3 synthesises the Reynolds and Strouhal number ranges.

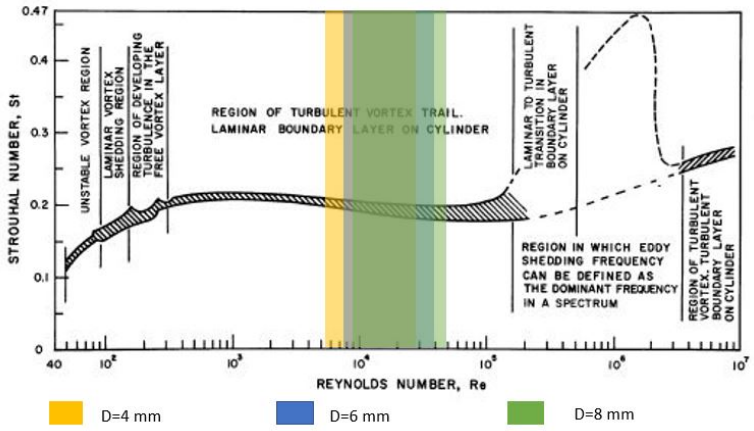

Figure 2.3: St Re correlation and range

2.3 Analytical aerothermal analysis

The propose of this section is to study analytically the heat exchange around cylinders. It is possible to calculate q (convective heat exchange) [W/m^2] as:

$$q = h(T_w - T_{aw}) \tag{2.3}$$

T_{aw} is the wall temperature when the heat flux is null, T_w is the real temperature of the wall. h is the convective heat flux coefficient. Very often it is convenient to use the Nusselt number; it is the non dimensional form of the h coefficient.

$$Nu = \frac{h \cdot D}{k} \tag{2.4}$$

k is the thermal conductivity of the considered fluid and D the cylinder diameter.

2.3.1 Pressure and temperature distribution

The first parameter useful to monitor is the pressure coefficient (c_p) on the cylinder wall. The formal definition of this coefficient is:

$$c_p = \frac{p - p_\infty}{\frac{1}{2}\rho V_\infty^2} \tag{2.5}$$

Using the potential theory it is possible to estimate the c_p coefficient as:

$$c_p(\theta) = 1 - 4sin^2(\theta) \tag{2.6}$$

From the literature we found some experimental data about the pressure around cylinders [27] [25]. Figure 2.4 shows a comparison between experimental incompressible data and c_p coming from potential flow theory. Until the separation point (in this case around 70 deg) the results coming from the two different approaches are quite similar; later the potential theory, is not able to predict the separation and the difference increases a lot. Also the Mach number can influence the pressure distribution around the cylinder.

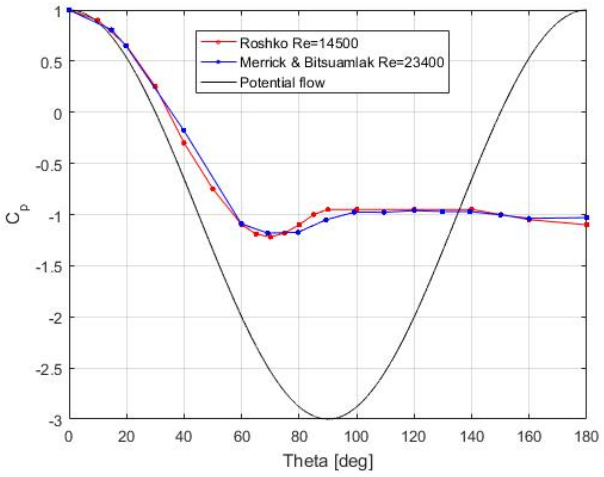

Figure 2.4: Comparison of c_p coming from different theories

Zhenhua and al.[38] studied numerically, with both LES and RANS techniques, this effect. Some results are presented in figure 2.5. At the stagnation point the evolution is isentropic so it is possible to use the following relation.

$$c_p(\theta = 0) = \frac{2}{\gamma M_\infty^2}\left[\left(1 + \frac{\gamma - 1}{2}M_\infty^2\right)^{\frac{\gamma}{\gamma-1}} - 1\right] \tag{2.7}$$

Figure 2.6 compares the results coming from equation 2.7 with results obtained from Zhenhua and al.[38], at the stagnation point.

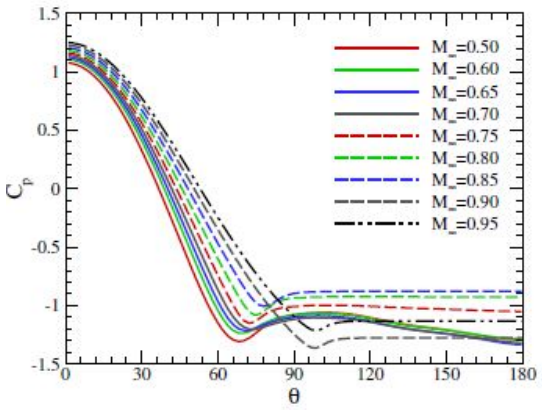

Figure 2.5: Effect of Mach number on the c_p around the cylinder surface

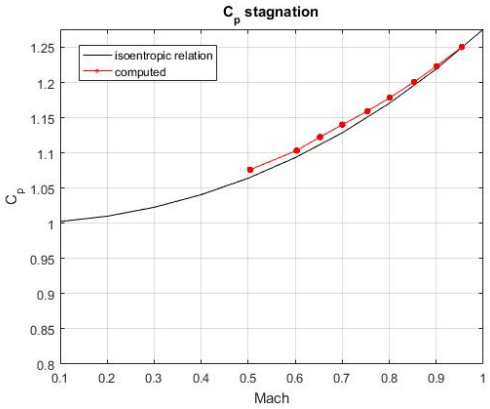

Figure 2.6: Effect of Mach number on the c_p at stagnation point

The final goal of this section is to estimate the adiabatic wall temperature distribution around the cylinder. Supposing isentropic evolution it is possible to write:

$$\frac{T_{aw}}{T^o} = R + (1-R)\left(\frac{p_e}{p_\infty}\right)^{\frac{\gamma-1}{\gamma}} \tag{2.8}$$

for incompressible flow:

$$\frac{p_e}{p^o} = c_p\left(1 - \frac{p_\infty}{p^o}\right) + \frac{p_\infty}{p^o} \tag{2.9}$$

with these formulas it is possible to obtain the recovery temperature distribution using the c_p distribution. R is the recovery factor; supposing a laminar flow evolution, at least in the cylinder forward part, as first approximation $R = \sqrt{(Pr)}$ can be used. White [37] proposed another approach. In this case the velocity distribution come from linearisation around the stagnation point (eq. 2.10), K is the velocity gradient at the stagnation point. In the incompressible approximation, using the Bernulli equation, the pressure around the cylinder is computed and finally the adiabatic wall temperature come form eq. 2.8

$$\frac{KD}{V_\infty} = 4 \cdot \left(1 - 0.416M^2 - 0.164M^4\right) \tag{2.10}$$

Figure 2.7 illustrates the recovery temperature distribution around the cylinder, calculated using the pressure distribution coming from the different, incompressible approaches

The last and most complete analytical approach consider also the effect of Mach number and flow compressibility. This approach is correct around the stagnation point. Korobkin et al. [16] propose a relation for the velocity around stagnation point

$$\frac{u}{u_\infty} = f(\theta) \tag{2.11}$$

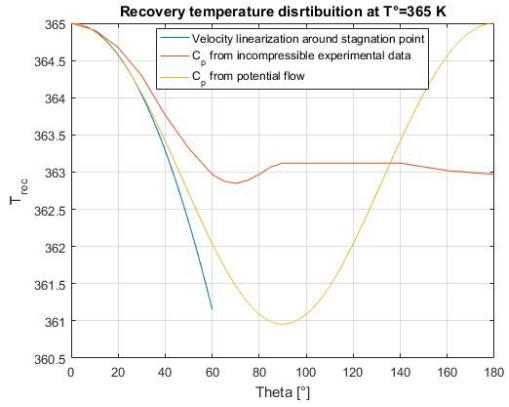

Figure 2.7: Adiabatic wall temperature around the cylinder

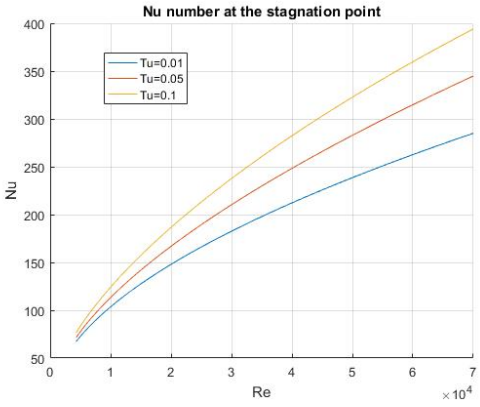

Figure 2.8: Nusselt number at the cylinder stagnation point

Using c_p definition, and substitute in eq.2.8 it is possible to obtain the equation 2.12

$$\frac{T_{aw}}{T^o} = R + (R-1)\,\frac{f^2(\theta)\,U_\infty^2 T_\infty}{2c_p T^o} \tag{2.12}$$

The term T_∞/T^o contains the Mach number influence. Figure 2.9 shows the trends coming from this approximation.

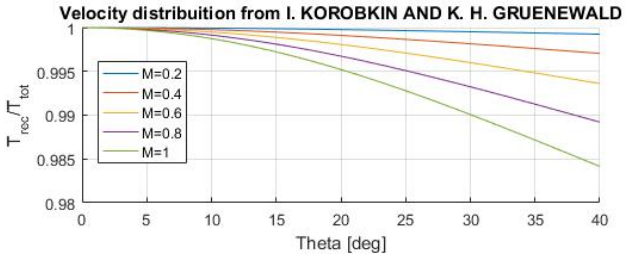

Figure 2.9: Mach influence on adiabatic wall temperature

2.3.2 Nusselt number

In literature does not exist theories able to estimate analitically the Nusselt number around a cylinder. The approach has to be empirical, experimental or numerical. G. W. Lowery[21] proposed an empirical formula able to estimate the cylinder Nusselt number at the stagnation point 2.13. This formula considers the effect of the Reynolds number and Turbulence intensity (TU). It is valid if the parameter $\sqrt{Re}TU$ is included between 0 and 64

$$\frac{Nu}{\sqrt{Re}} = 1.010 + 2.624 \cdot \left(\frac{Tu \cdot \sqrt{Re}}{100}\right) - 3.070 \cdot \left(\frac{Tu \cdot \sqrt{Re}}{100}\right)^2 \tag{2.13}$$

Figure 2.8 presents the results at the stagnation point obtained using eq. 2.13. The heat

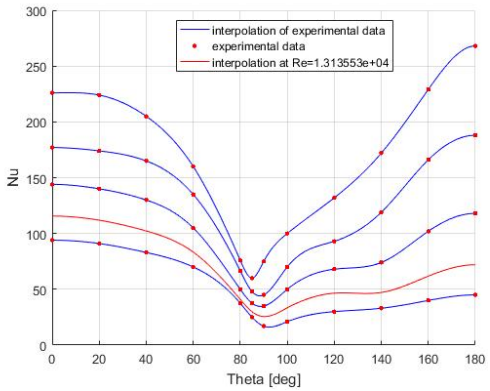

Figure 2.10: Local Nusselt number distribution around the cylinder

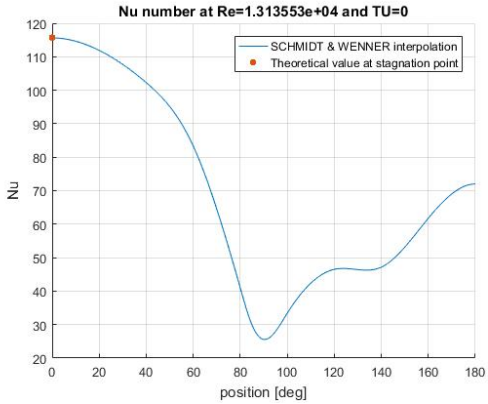

Figure 2.11: Comparison between Nu at the stagnation point and the distribution around the cylinder at $Re = 1.3 \cdot 10^4$

exchange increases with Reynolds number, but also with the turbulence intensity. The final problem is to estimate the local Nu number around a cylinder. Some experiments are carried out by Schmidt et al.[30]. They studied the local forced convection at different Reynolds number and low turbulence intensity. With a double variable interpolation we used their experimental results to estimate the Nusselt number at our Reynolds (fig 2.10). It possible to validate, at the stagnation point, the Schmidt results using the eq.2.13. Figure 2.11 presents the results of this process. Great congruence is present, in our flow conditions (Re=131355 and TU=0.2%), between Lowery formula and the interpolation coming from Schmidt et al. experimental results.

2.4 CFD analysis

The previous section presents results coming form experiment and empirical formulations. They are very useful for estimating the general behaviour and obtaining some data useful for the validation of experimental and numerical results. In this section we want to create a numerical 2D model able to simulate, with good accuracy, the fluid around the probe. All the CFD calculation are carried out with ANSYS. We used ICEM cfd for the mesh construction and FLUENT for the field solution. The first part of this section describes the general numerical set up; the second one the steady state results and the last one presents the results coming from unsteady simulations.

2.4.1 Numerical set-up

In order to create a good mesh we analysed some examples from literature are analysed. Table 2.4 summarises all the analysed meshes. A first, draft mesh was created, but when

the calculations are launched it seemed that a boundary influence was present on the fluid dynamics field; therefore a greater domain mesh is built. The final computed mesh contains 72125 cells in a $26D \times 39D$ domain. The dimension of the first cells near the wall are arround $1 \cdot 10^{-4}$D in order to reach a $y^+ \approx 0.1$ for the first cell center (Suggested value by Fluent Theory Guide [11]). Figure 2.12 shows a general schema representing the mesh. For this analysis we use a RANS approach in order to limit the computational cost. With

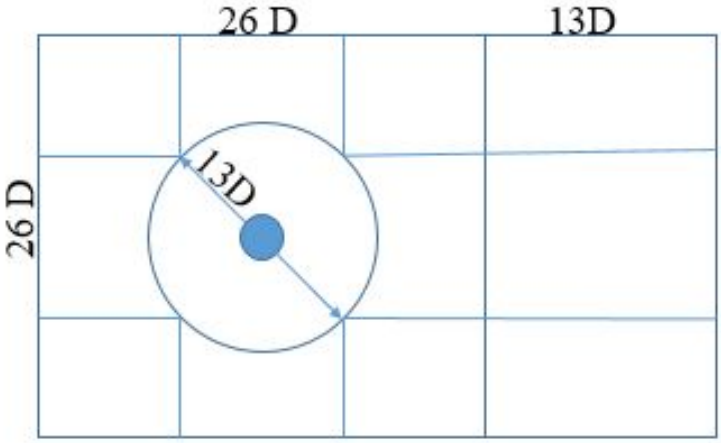

Figure 2.12: Schema representing the computed mesh

RANS it is possible to obtain accurate results, but the critical point is the selection of the turbulence model. Fluent offers a lot of options and we tested two different models. The first one is the SST transitional model; it is based on a classical $k - \omega$ model, two equations, one for turbulent kinetic energy and one for the dissipation rate ω are solved. In this case two additional equations are implemented, one for turbulence intermittency γ (the probability that a given point is a turbulent point) and one for the transition criteria (Momentum thickness Reynolds number)[11]. The second considered model is the RSM (Ryenolds Stress Model). It is the most powerful and computational expensive Fluent turbulence model. This model abandons the Businnesq hypothesis (isotropy of Reynolds stress tensor) and 5 equations, 4 for Reynolds stress tensor elements and one for dissipation rate are solved[11]. The SST transition model is less accurate than the RSM model, but the second one is computationally more expensive and the convergence achievement is more delicate. For the steady state case the SST transition model is used, starting from this solution the unsteady simulations with RSM are launched.
It is important to define the boundary conditions type. On the left side the pressure inlet condition is chosen, Fluent requires to indicate the total pressure and the total temperature. At the outlet boundary the static pressure and the total temperature are fixed with the outlet pressure condition. Fundamental is also to impose correctly the turbulence parameters at inlet and outlet. In particular we fixed:

Paper	Re number	N cells	Mesh type	Dominium size	First cell	Turbulence model	c_d	time step [s]
Kulyakhtin et al[17]	$1.6 \cdot 10^4$	10496	structured	$16D \cdot 24D$	0.06D	k-ϵ wall velocity law	0.24	steady
Kulyakhtin et al[17]	$1.6 \cdot 10^4$	41728	structured	$16D \cdot 24D$	0.001D	k-ϵ boundary solution	0.515	$2.5 \cdot 10^{-5}$
Kulyakhtin et al[17]	$1.6 \cdot 10^4$	41728	Structured	$16D \cdot 24D$	0.001D	SST transition	1.66	$2.5 \cdot 10^{-5}$
Shao et al[33]	$5.3 \cdot 10^3$	15885	unstructured	$16D \cdot 30D$		k ϵ model	0.64	$1 \cdot 10^{-4}$
Vaz et al [36]	$9.4 \cdot 10^4$	161465	structured	$7D \cdot 20D$	$y^+ \approx 1$	RSM	0.864	$1 \cdot 10^{-2}$
Vaz et al [36]	$9.4 \cdot 10^4$	221325	structured	$7D \cdot 20D$	$y^+ \approx 1$	k ω SST transition	0.834	$1 \cdot 10^{-2}$
Vaz et al [36]	$9.4 \cdot 10^4$	221325	structured	$7D \cdot 20D$	$y^+ \approx 1$	RSM	1.068	$1 \cdot 10^{-2}$
Bonetti [3]	$3 \cdot 10^3$	242398	unstructured	$20D \cdot 30D$	$y^+ \leq 1$	Spalart-Allmaras	1.30	$1 \cdot 10^{-6}$
Computed steady	$1.3 \cdot 10^4$	52362	structured	$16D \cdot 24D$	$1 \cdot 10^{-4}D$	SST transitional	0.80	steady
Computed steady	$1.3 \cdot 10^4$	72125	structured	$26D \cdot 39D$	$1 \cdot 10^{-4}D$	SST transitional	0.81	steady
Computed	$1.3 \cdot 10^4$	72125	structured	$26D \cdot 39D$	$1 \cdot 10^{-4}D$	RSM	1.10	$1 \cdot 10^{-5}$

Table 2.4: Mesh examples

- Turbulence intensity: 0,2% (typical for wind tunnel)
- Turbulence Intermittency: 1 [11]
- Turbulent viscous ratio μ_t/μ: 10 [11]

On the lateral boundaries, we imposed the symmetry condition. On the wall surface the non slip condition is imposed for the velocity field and; in this case, null heat flux (adiabatic simulation) as thermal condition. An overview of all the boundary condition is presented in figure 2.13
In the following list summarises all the setted parameters for the steady state simulation:

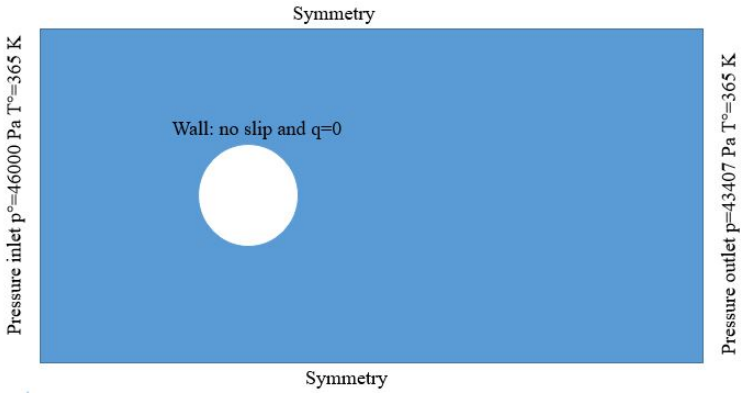

Figure 2.13: Boundary conditions

- Diameter D=0,006m
- Reynolds number: $Re = 1,3 \cdot 10^4$
- 2D compressible flow
- Pressure based algorithm (suggested for low Mach compressible flow [11])
- Ideal gas law for the system closure
- Sutherland law for the viscosity
- Turbulence transition SST model
- Mesh requirement: $0.001 < y^+ < 1$ [11]
- Second order upwind numerical method
- Converge if $residuals < 1 \cdot 10^{-3}$
- Viscous heating: include in the energy equation the term due to viscous heating

2.4.2 Steady state solution

The actual field is strongly unsteady therefore it is impossible to find a converged, steady state solution (the simulation does not converge). During the iterations, the integral variables C_l and C_d (and also the residuals) begin to oscillate.

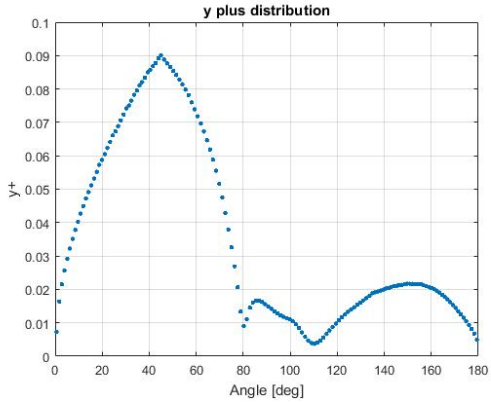

Figure 2.14: y^+ first cells near wall distribution

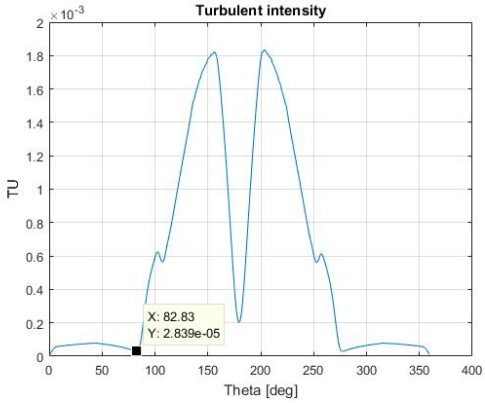

Figure 2.15: Turbulence intensity distribution first cell near wall

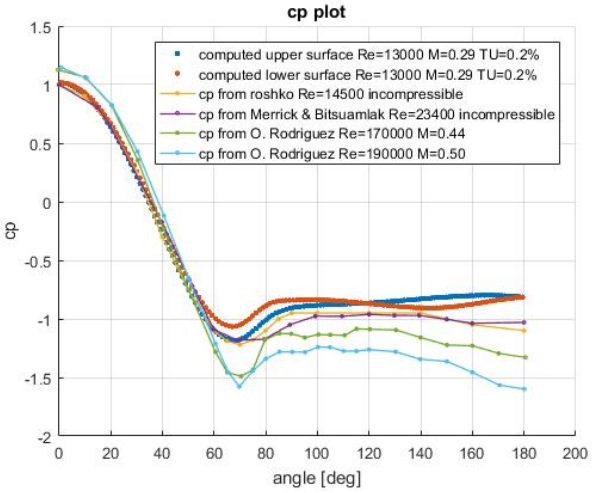

Figure 2.16: C_p at wall steady comparison

Table 2.5 shows some important variables coming from the simulation compared with the same kind of values, expected from theoretical or experimental theories. Figure 2.14 presents the distribution of y^+ corresponed to the coordinate of the first cell near wall. As it is suggested by the Fluent User Guide[11] this parameter ranges between 0.001 and 1 for all wall position. Figure 2.16 shows the c_p trend along the whole cylinder

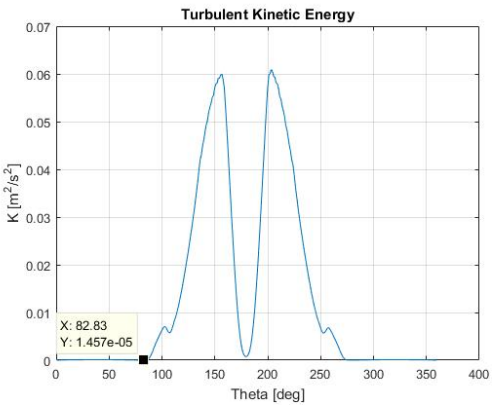

Figure 2.17: Turbulent kinetic energy first cells near wall

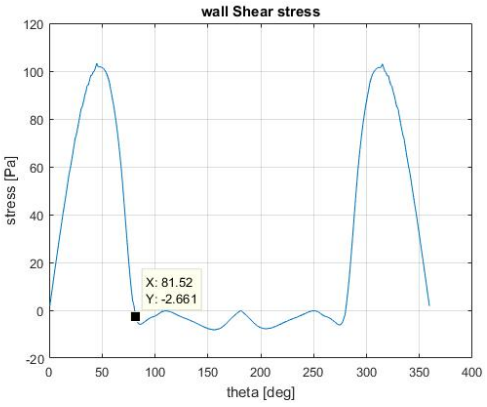

Figure 2.18: Wall shear stress distribution on the cylinder surface

Variable	Computed value	Expected value	Theory
M_∞	0.2840	0.2891	Isentropic theory
C_p stagnation	1.023	1.021	Isentropic theory
C_D (Drag)	0.953	1.040	White [37]

Table 2.5: Computed expected comparison

wall. The computed values are compared with some results coming from the literature (Roshko [27], Merrick et al. [25], Rodriguez [26]). The pressure is not the same on both the cylinder sides because the steady convergence is not reached. The computed values are similar to the experimental incompressible results (the simulation Mach number is low). The mathematical model over estimates the pressure recovery in the backward part of the cylinder. This effect is also visible in the C_d value (table 2.5). The computed pressure recovery is larger than the real one, for this reason also the C_d computed with the simulations is lower than the C_d coming from the experimental data.

Figures 2.15, 2.17, 2.18 show respectively the turbulence intensity and the turbulent kinetic energy near the wall (first cell) and the wall shear stress on the cylinder surface. When the wall shear pass from positive to negative value the separation occurs, in this case the separation is located at 82 deg. (Zhenhua et al. [38] predict the separation at $\theta_{sp} \approx 80$). As it is expectable in this Reynolds range, a laminar separation occurs; before 82 deg the boundary layer is laminar, in fact the turbulence intensity and the the turbulent kinetic energy are very low. As soon as the boundary layer separates, the turbulence level increases a lot and therefore also these parameters increase. In correspondence of the separation point the wall shear stress became negative (figure 2.18). This underline the presence of inverse flow region. This is confirmed by plotting the streamlines near wall (figure 2.19). For the steady state simulation the temperature distribution is not presented because it is completely different respect to the expected

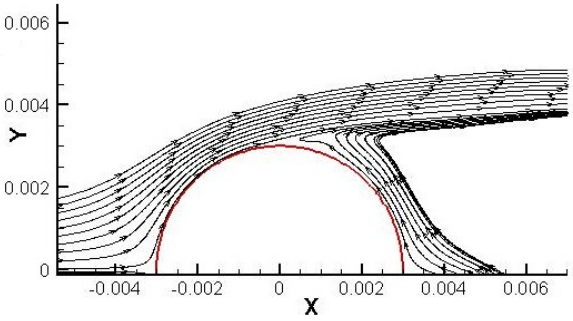

Figure 2.19: Streamlines near wall $Re = 1.3 \cdot 10^4$

experimental values [29] [14]. This because the temperature distribution is strongly affected by the the unsteady structures that influence the convective phenomena but, are not predicted by the steady state simulation [14].

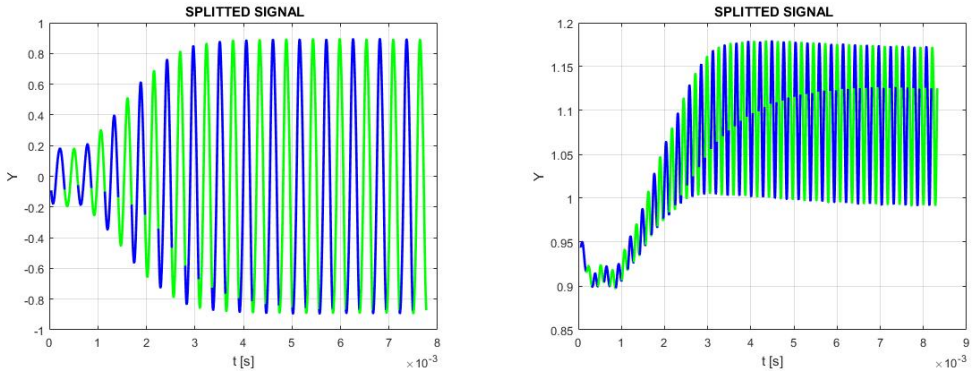

Figure 2.20: Lift and drag time histories

2.4.3 Unsteady adiabatic simulation

Starting from the steady state solution the unsteady simulation is launched. In this case the RSM (Reynolds Stress Model) is used for the Reynolds shear tensor modelling. In general this model is considered more accurate than the SST transition but the convergence could be reached only in the unsteady case, initializing the simulation with stationary results. The chosen time step is $1 \cdot 10^{-5} s$; this is selected, starting from the shedding frequency estimation 2.3, in order to have more than 25 time step each vortex shedding period. The field is unsteady and it is difficult to understand when the system oscillations reached their regime. To estimate this unsteady convergence some parameters are defined [3]:

- $fM = 1 - \left|1 - \frac{\overline{q_{i+1}}}{\overline{q_i}}\right|$

- $fA(f_{int}) = 1 - \left|1 - \frac{\|ft(f_{int})_{i+1}\|}{\|ft(f_{int})_i\|}\right|$
- $fphi(f_{int}) = 1 - \left|1 - \frac{phase(ft(f_{int})_{i+1}) - phase(ft(f_{int})_i)}{\pi}\right|$
- $fs = \frac{\frac{1}{N}\sum_{n=1}^{N} q'(n)q'(n+N)}{\frac{1}{N}\left[\sum_{n=1}^{N} q'^2(n) \sum_{N}^{n=1} q'^2(n+N)\right]^{1/2}}$
- $fP = \frac{PSD(f_{int})}{\sum_{k=1}^{N} PSD(k)}$

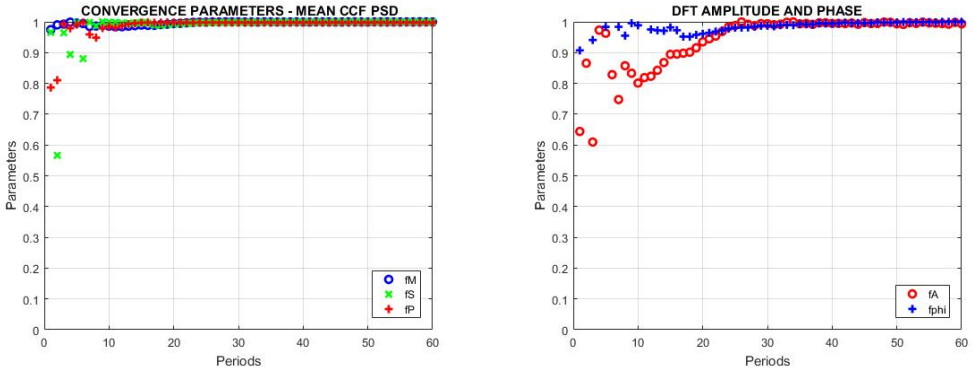

Figure 2.21: Parameter histories using C_d signals

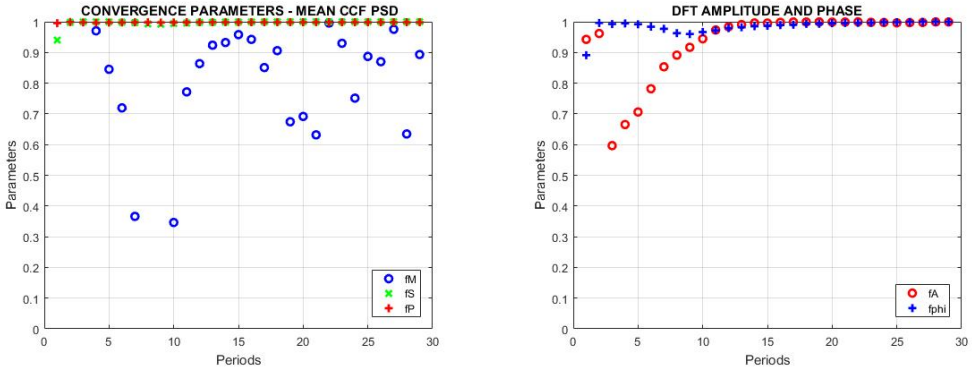

Figure 2.22: Parameters history using C_l signals

q is a general variable; in this analysis we check the convergence calculating the parameters with different integral and local variables (C_l, C_d, pressure and temperature at different wall points). q' is the fluctuation of q around its mean value, f_{int} is the most powerful frequency in the q' spectrum. N is the number of samples in each period. The parameter fM compares the mean value of q in two adjacent periods; the parameters fA and $fphi$ compare the amplitude and the phase associated at the main frequency in two adjacent periods. fs estimates the cross correlations of signal in two adjacent

periods and fP gives informations about the energy at the main frequency compared with the total energy contained in the signal. Theoretically the convergence is complete when all these parameters all equal to 1. Clark and Grover [8] conclude that the simulation could be stopped when all these parameters are greater than 0.95. Both local (c_p and temperature at θ equal to 0, 45, 90, 135 and 180 degrees) and integral (C_l and C_d) variables time histories are selected for evaluating the unsteady convergence. For each time history the spectrum is calculate and the dominant frequency is selected, the signal is split in periods and for each period the six parameters are calculated. Figure 2.20 shows the lift (C_l) and drag (C_d) signals split in periods. It is possible to plot the six parameters calculated using drag and lift coefficients (figure 2.22). The same procedure is repeted for all the selected variables. All the parameters are larger than 0.95 as required by [8]. The only one, seems not converging, is the fM calculated with C_L. This because the mean lift is equal to zero, so when we calculate fM we have a 0/0 indeterminate form which make fM parameter extremely sensitive at numerical errors and for this reason, in this case, could be discarded. When the simulation converges the calculation is launched for some more periods. On this additional data all the unsteady analysis are computed.
Figure 2.23 and 2.24 present the time histories and the spectra of C_d and C_l coefficients.
The numerical model is able to capture very well the vortex shedding phenomena. The

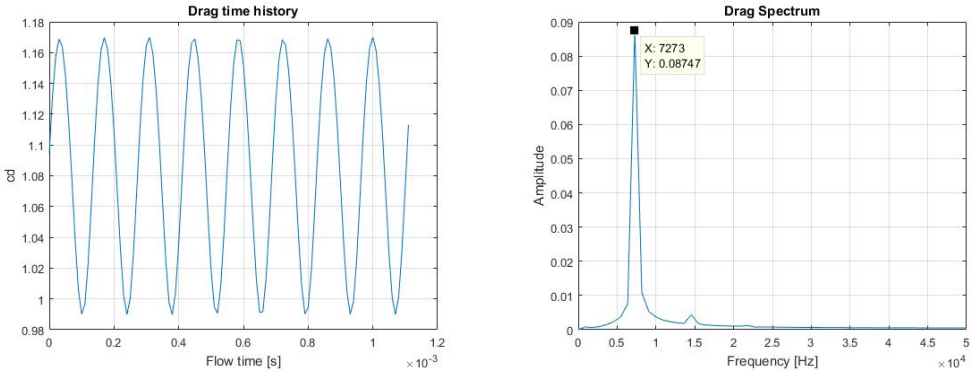

Figure 2.23: Drag time history and spectrum

Lift spectrum present a peak corresponding at the vortex shedding frequency. This frequency (3636 Hz) is very close to the vortex shedding frequency theoretically predicted in table 2.3. The drag spectrum present a maximum at the double frequency. This because a period in the drag time history corresponds at one vortex detachment. The lift makes a cycle, in his time history, every time 2 vortexes detachment (one by each cylinder surface side). The vortexes leave each cylinder side in phase opposition, this explains the double frequency in drag spectrum.
In order to well understand the general flow arrangement it is important to plot the mean velocity field magnitude with the streamlines (figure 2.25). The geometry and the boundary conditions are, symmetrical so also the mean velocity field is symmetrical

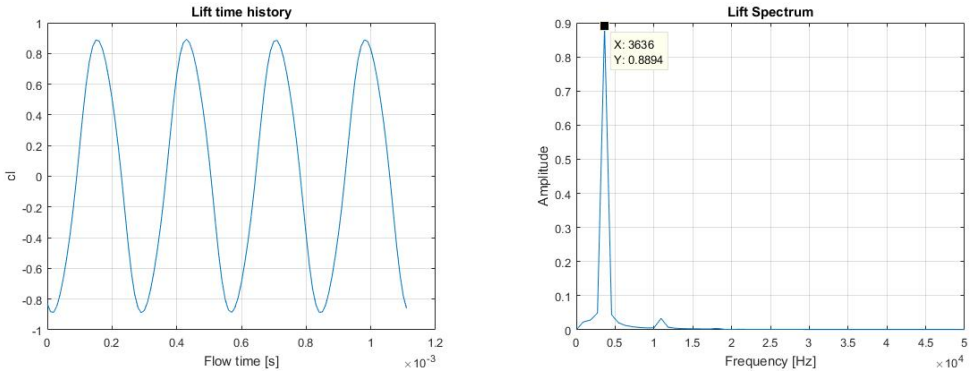

Figure 2.24: Lift time history and spectrum

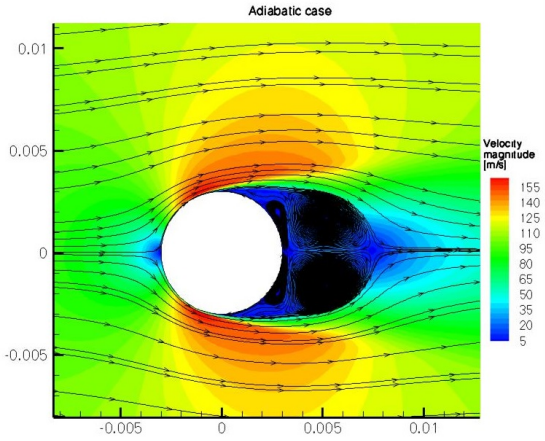

Figure 2.25: Mean velocity field around the cylinder

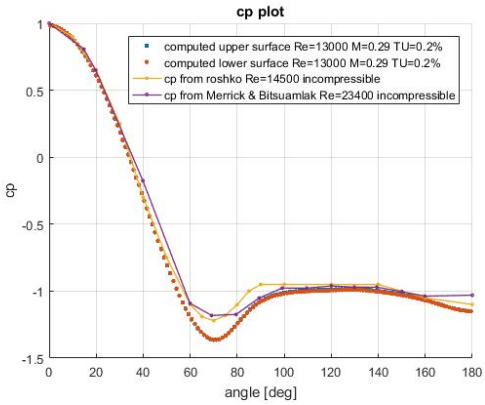

Figure 2.26: Mean c_p on the cylinder surface

respect to the cylinder y axis. Around 82 deg the separation point is underlined by a reverse flow zone, later the flow reattach at more or less 140 deg. This phenomena creates four symmetrical recirculation bubbles in the cylinder, mean wake. It is possible to plot the mean c_p on the wall (fig 2.26); the results are very similar to the trends measured experimentally. [27] [25]. In order to validate the unsteady solution, we launched the simulation with the same conditions experimented by Rodriguez (Re=170000 M=0.40) [26]. It is possible to calculate the pressure coefficient spectra for all points on the wall. For each point, we can obtain the oscillation amplitude at the dominant shedding frequency. Finally, if these amplitudes are plotted along the cylinder wall, a comparison between the computed and the measured [26] amplitudes is possible. (fig 2.27) This comparison shows a very good correlation between numerical and experimental data until the separation point. Later the difference increase, this could be caused by the

great influence that the inlet turbulence intensity has on the separation phenomena. In

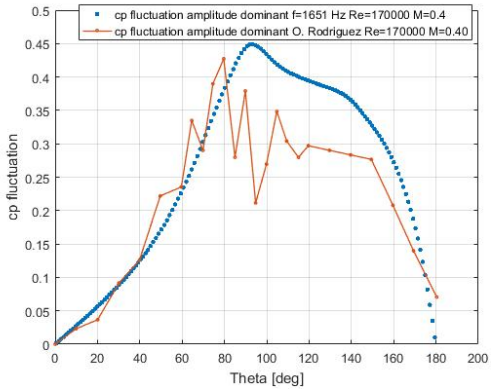

Figure 2.27: c_p fluctuation amplitude at shedding frequency

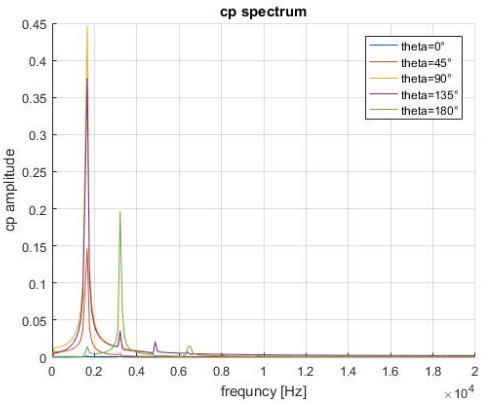

Figure 2.28: c_p spectra

the same conditions is also possible to plot the pressure coefficient spectra in different points.(figure 2.28) The spectra present a peak in correspondence of dominant shedding frequency. Only at 180 degrees the highest peak is located at double frequency; this because, in this point, it is possible to hear the vortexes that alternatively detach from both the cylinder sides. The last monitored parameter for the numerical model validation is the energy separation factor defined as:

$$S = \frac{T_{aw} - T^o}{\frac{U_\infty^2}{2c_p}} \tag{2.14}$$

In this case we use the mean temperature on each point on the cylinder surface. The results compared with experimental data coming from R. J. Goldstein et al [14] (Re = 51570) and S. Sanitjai et al [29] (Re = 63380) are showed in figure 2.29
The model is now validated, it is possible to use the mean temperature distribution for estimating the error ,made by the probe, in the total temperature measurements. From the fluid dynamics point of view, there are three different sources of error: the error due to the flow misalignment, the error due to integral effect of the sensor (figure 2.30) and the error due to the temperature fluctuations generated by vortex shedding. Generally the error is defined as

$$error = T^o - \frac{1}{L}\int_L T_{aw} dL \tag{2.15}$$

where L is the sensor dimensions. In normalized form the error became

$$error = \frac{T^o - \frac{1}{L}\int_L T_{aw} dL}{T^o} \tag{2.16}$$

Figure 2.31 shows the error, on the total temperature measurement, due to flow misalignment for 3 different sensor dimensions. Figure 2.32 illustrates the error at the stagnation

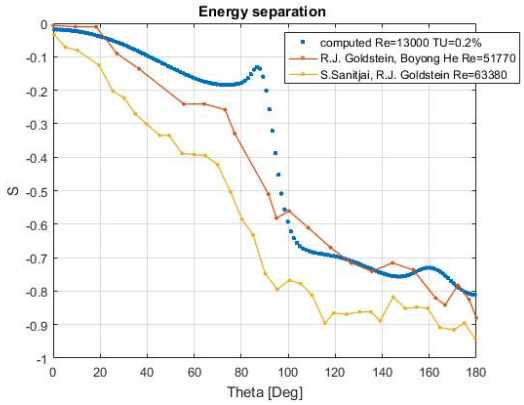

Figure 2.29: Mean energy separation factor

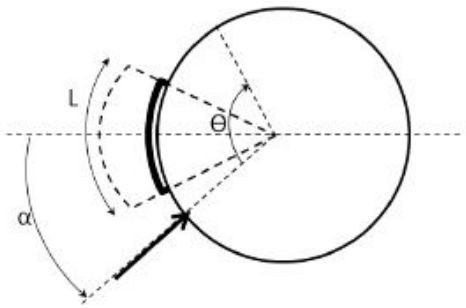

Figure 2.30: Schema of the probe with the sensor

point due to the integral effect of the sensor. For both these analyses it is used the mean adiabatic wall temperature distributions coming from the adiabatic unsteady simulation. Finally figure 2.33 shows the error due to the temperature fluctuation at two different

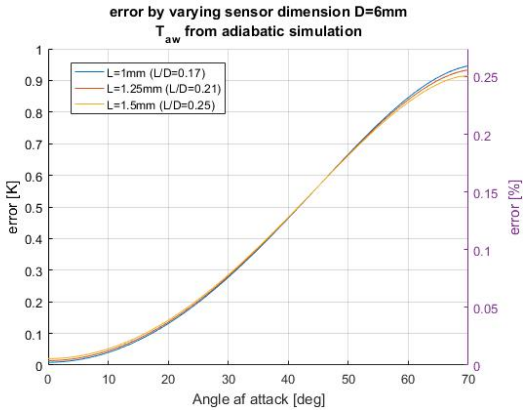

Figure 2.31: Error due to flow misalignment different sensor lengths

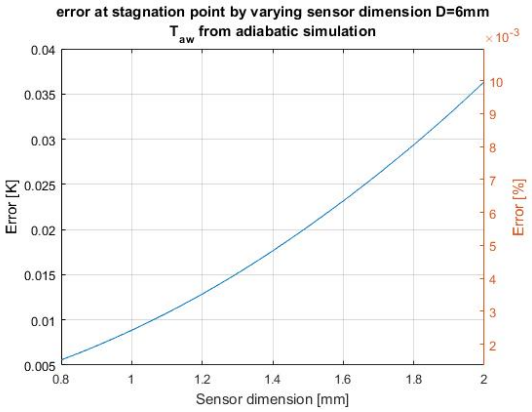

Figure 2.32: Error at stagnation point due to sensor integral effect

frequencies. ($f_{shedding}$ and $2f_{shedding}$).

Concluding with the adiabatic simulation we are able to obtain the distribution of the adiabatic wall temperature. Using this spatial and temporal distribution ($T_{aw}(t,\theta)$) it is possible to estimate the probe error. If the flow attach angle remains less than 70 degrees the error on the mean total temperature measurement is lower than 1 K at $T^o = 365K(0.25\%)$ fig.2.31. The integral effect of the sensor is very low, 0.04 K if the sensor dimension is lower than 2mm. The most dangerous error source seems to be the vortex shedding. This phenomena can create oscillations, in the adiabatic wall temper-

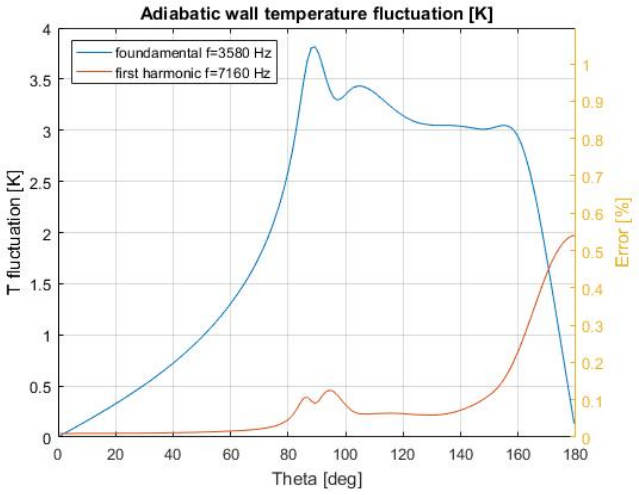

Figure 2.33: Error due to vortex shedding, dominant and first harmonic frequencies

ature, that can go back and influence the thermal field in the cylinder forward part. For attack angle between 0 and 80 degrees the temperature oscillations remain between 0 and 2.5 K. Luckily these oscillations have very specific frequency (vortex shedding frequency), so it is possible to filtrate the signal coming from the probe and limiting this effect.

2.4.4 Wall temperature influence on heat exchange

With the previous analysis we created and validated a numerical model able to simulate the thermal field around a cylinder. Now, the principal goal of this section, is to understand how different wall temperatures can influence the heat flux phenomena. We want to verify the convective heat flux law (eq.2.17)(positive heat flux is coming out from the cylinder) and the predicted linearity in the heat exchange. Finally we want to develop a procedure able to considerate the non linear effects in the wall heat exchange.

$$q = h(T_w - T_{aw}) \tag{2.17}$$

The simpler procedure for understanding the phenomena, is to launch some simulations with isothermal wall condition at different wall temperature. For each simulation we should impose a temperature at wall ad calculate the heat flux, by comparing the heat flux at different temperatures it is possible to estimate the adiabatic wall temperature an the local Nusselt number. Unfortunately Fluent, in case of isothermal wall condition, calculates the heat flux in a very particular and unreliable method. The software estimate an h_f coefficient and, using the local fluid temperature (T_f) and the wall temperature (T_W), calculates the heat flux as [12]:

$$q = h_f(T_w - T_f) \tag{2.18}$$

We need a more accurate estimation of heat flux so this approach can not be used. For solving this problem we launched some simulations imposing different heat fluxes on the cylinder wall. From each simulation we extract the wall temperature distribution; knowing the wall temperature at different heat flux conditions, it is possible to calculate the local Nusselt number and to reconstruct the adiabatic wall temperature histories for each wall cylinder point ($T_w(\theta, t)$). Before make any kind of analysis, it is required to synchronize the the output signals coming from the iso heat flux simulations. We choose to synchronize the fluid dynamics fields and the selected variable for the synchronization is the pressure at wall. In order to calculate the time shifting between the two fields signals, a cross correlation parameter is defined (eq. 2.19). The Δt corresponded at the maximum P, cross parameter, represents the time offset between the two signals.

$$P(\Delta t) = \frac{1}{signallength} \sum_{\theta} \sum_{t} p_1(t, \theta) \cdot p_2(t + \Delta t, \theta) \tag{2.19}$$

Two iso heat flux simulations are launched at $q = 3000$ W/m^2 and $q = -3000$ W/m^2. When the signals are synchronized, for each time step and for each surface point, using linear interpolation, it is possible to calculate the instantaneous, local adiabatic wall temperature. Figure 2.35 illustrates an example of this interpolation, at fixed time step, for some surface points. Finally the computed time history is averaged in time and the results are compared with the local mean T_{aw} coming from the adiabatic simulation (figure 2.36). Figure 2.34 shows a schema presenting the complete process is presented in . It is also interesting to plot the evolutions of mean temperature around the

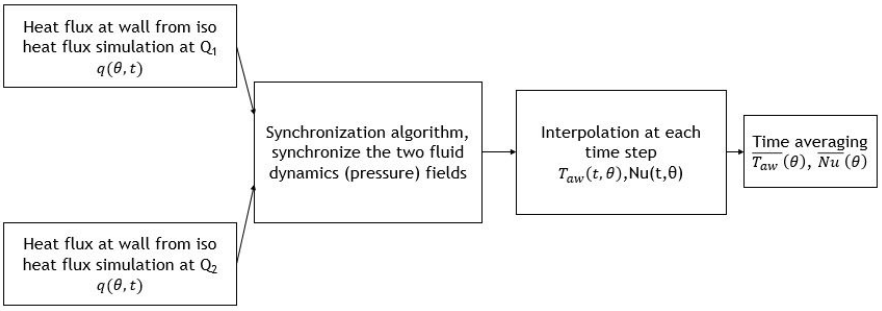

Figure 2.34: Developed interpolation algorithm

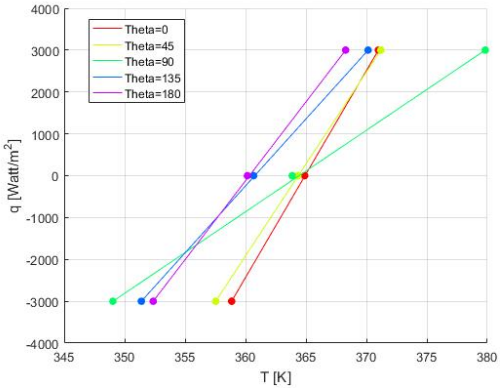

Figure 2.35: Example of linear interpolation heat flux vs temperature

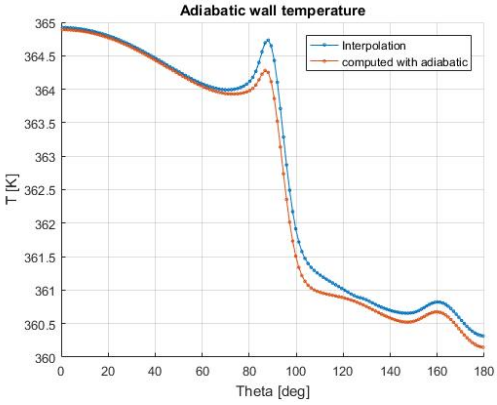

Figure 2.36: Comparison between the adiabatic wall temperatures calculated with differer approaches

cylinder (fig2.37) in the three cases ($q = -3000W/m^2$, $q = 3000W/m^2$, $q = 0W/m^2$). We notice that when the difference between the temperature increase, also the error in T_{aw} interpolation is increasing. Using the same approach is possible to obtain, at each time step, the Nusselt number distribution around the cylinder surface. Using these data we calculate the time average Nusselt number distribution. In figure 2.38 we compare the obtained mean Nu with some experimental results[30] [24]. Near the stagnation point the computed and the experimental data are very similar. At $\theta \approx 60deg$ the error starts to increase. The cause could be the high influence of turbulence intensity on the heat flux (the two experimental studies don't considered this factor). Another cause could be the influence of the flow temperature on the heat flux coefficient h [19]. It is very interesting to evaluate the fluctuations of Nusselt number around the cylinder surface. The fluctuations associated at the fundamental and at the first harmonic are plotted in the figure 2.39. Luckily the Nusselt fluctuations are very low (under 2.5) if the attack angle is lower than 60 deg. At the fundamental vortex shedding

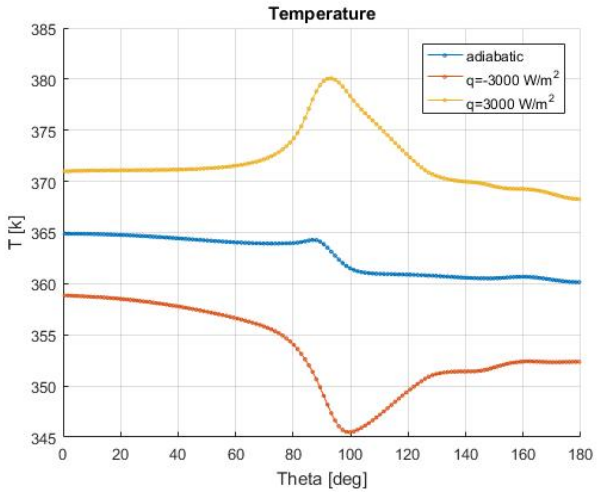

Figure 2.37: Comparison between wall temperature for iso heat flux simulations

frequency the Nu fluctuations present a maximum near the separation point; downstream the fluctuation amplitude is reducing, begins to regrow and has another peak near the reattached point. For the first harmonic the fluctuation amplitude remain very low along the main part of cylinder surface, only along the backward cylinder part (later than 140 deg) this amplitude grows up. In this case the trend is very similar to the adiabatic wall temperature fluctuations.
The last point of this section is to understand how the non linear effect can influence the heat flux phenomena. Lavagnoli et al [19] proposed a correction, on the linear convective heat flux law, taking into account two effects. The first one considers the changing in flow proprieties and h coefficient with the temperature:

$$h = h_0 \left(\frac{T_w}{T_{aw0}} \right)^n \tag{2.20}$$

the second effect considers the flow time history. Changing the wall temperature the flow is heated or cooled; the temperature of the flow in a fixed point is influenced by the wall temperature in the previous points. Changing the wall temperature, the temperature of the flow is different and the convective phenomena is influenced. The complete correction law is:

$$q = h_0 \cdot \left(\frac{T_w}{T_{aw0}} \right)^n \left(T_{aw0} - T_w + k \cdot sign(T_w - T_{aw0}) \cdot (T_w - T_{aw0})^2 \right) \tag{2.21}$$

In order to investigate these effects other iso heat flux simulations at $q = -3300 W/m^2$ and $q = 3300 W/m^2$ are launched. In this case the post process approach is a little bit different. We do not use the algorithm summarized in figure 2.34 but a simplified post processing procedure. The local wall temperature fields, coming from the unsteady simulations, are averaged in order to obtain, for each simulation, the mean, local wall

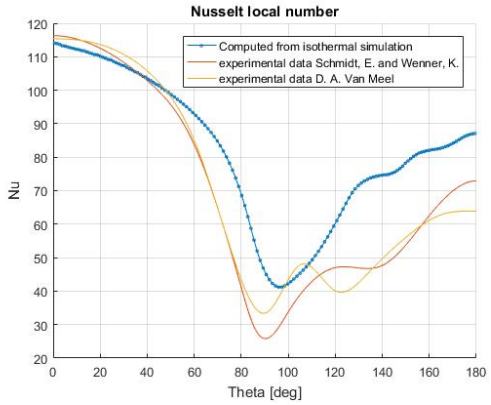

Figure 2.38: Comparison between computed and experimental Nusselt

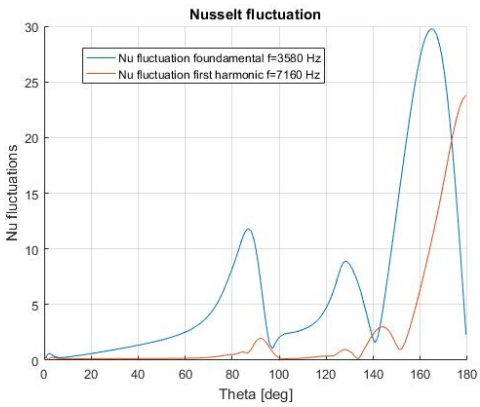

Figure 2.39: Nusselt fluctuations at the fundamental and second harmonics

temperature distribution around the cylinder. The linearisation procedure is carried out with the mean temperature distribution and not, each time step, using the instantaneous wall temperature values. This method is simpler and allows to better understand how the linearisation procedure works. This simplified procedure is tested also on the data coming form $q = 3000\mathrm{W/m^2}$ and $q = -3000\ \mathrm{W/m^2}$ the results do not present appreciable differences.

The averaging procedure is a critical point, and has to be very accurate. A small error on the mean wall temperature could cause great error in adiabatic wall temperature and Nusselt number estimation, in particular if the selected wall temperatures are very close and different from the desired adiabatic wall temperature. When the procedure is carried out, for obtaining the real mean wall temperature, it is important to isolate an integer number of vortex shedding periods in the time histories. The problem is that the vortex shedding frequency is not exactly the same around all parts of the cylinder wall. This problem is solved by using the symmetry of the fluid dynamics field, and meaning the time average wall temperatures, between the left and the right side of the cylinder surface. The figure 2.40 shows the linearisation procedure, in some point on the cylinder surface. With this interpolation it is easy to detect the first non linear effect that causes the changing in the local heat flux/temperature slope. The interpolation procedure is carried out with different methods: linear using the wall temperatures at $q = -3000\ \mathrm{W/m^2}$ and $q = 3000\ \mathrm{W/m^2}$, linear using the wall temperature at $q = -3300\ \mathrm{W/m^2}$ and $q = -3000\ \mathrm{W/m^2}$, linear using the wall temperature at q=3000 W/m^2 and q=3300 W/m^2, non linear using the equation 2.21 and solving the non linear system with the Matlab routine $nlinfit$; in the last case the convergence is guarantee by monitoring the residuals. Considering all points on the cylinder surface the maximum residual for the non linear system is $2.25 \cdot 10^{-10} W/m^2$; the convergence is reached. The figure 2.41 compares the adiabatic wall temperatures on the cylinder wall, obtained with the four different methods, with the adiabatic wall temperature coming from the adiabatic

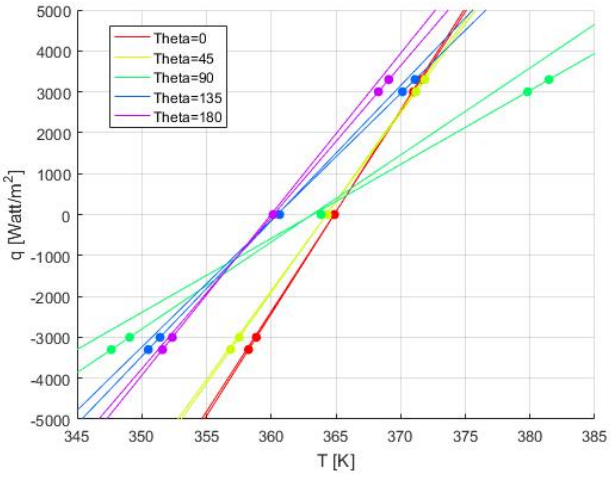

Figure 2.40: Example of linear interpolation in different wall point

simulation.

Until 60 deg all the computed temperature are very similar. When the angle of attack increase the linear methods, if compared with the adiabatic case, can overestimate or underestimate the temperature. The maximum error can reach also 0.5 K. The adiabatic wall temperature computed with the non linear four coefficient approach works very well and can follow accurately the wall temperature computed with the adiabatic simulation. It is possible to plot the Nusselt number computed with different approaches: the first one evaluating the slope of heat flux / temperature (h coefficient) using the data coming from the simulations at q=-3300 W/m^2 and $q = -3000$ W/m^2 the second using data coming from simulations at $q = 3300$ W/m^2 and $q = 3000$ W/m^2 and the last one calculation the Nu using the h_0 coefficient coming from the non linear interpolation (eq. 2.21). Figure 2.42 shows the results, varying the angle, on the cylinder surface. The values of Nusselt computed with the non linear approach range between the values obtained with the linear approaches at positive and negative heat flux. If the wall temperature increase the Nusselt number decrease, for this reason the expected n coefficient is negative. It is also very interesting to plot the local coefficients n and k on the cylinder surface. (eq. 2.21). In figure 2.43 it is plotted the n coefficient; until the separation point it is around n=-0.3. According to the literature [19] this coefficient, for the flat plate, should be between 0 and -0.4 depending from the turbulence level (0 for laminar flow). The k coefficient (figure 2.44) is very low and increases only in the backward part of the cylinder where the influence of flow time history became important.

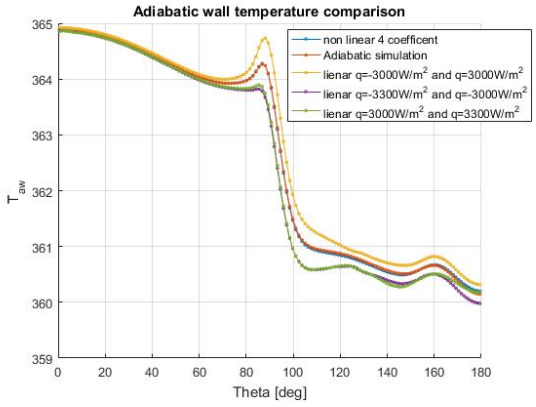

Figure 2.41: Comparison between adiabatic wall temperatures obtained with different methods

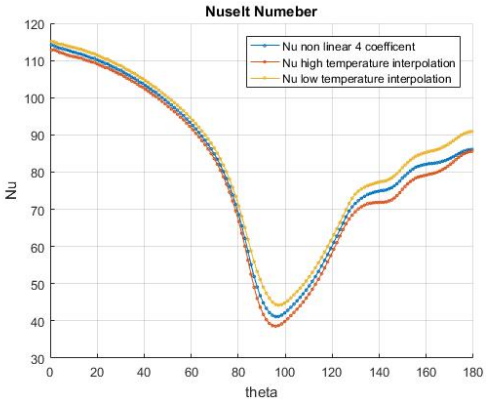

Figure 2.42: Comparison between Nusselt numbers obtained with different methods

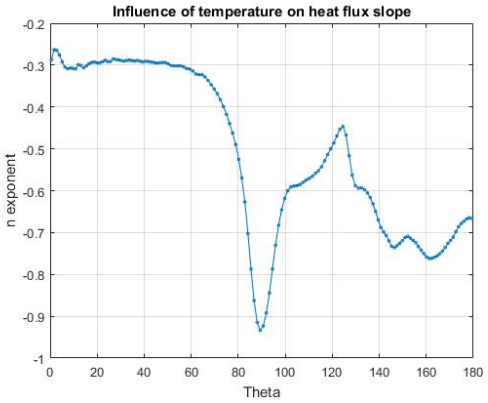

Figure 2.43: n coefficient computed around the cylinder surface

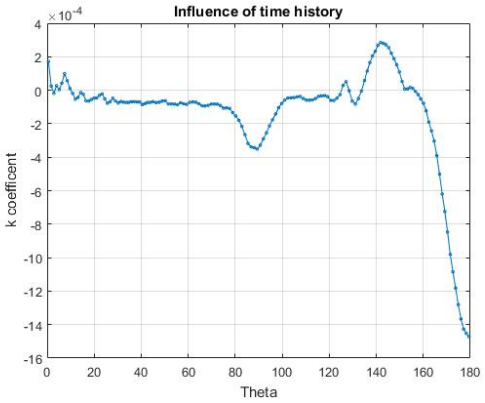

Figure 2.44: k coefficient computed around the cylinder surface

2.4.5 Real high turbulence case

The final probe has to work behind the CT3 rotor. In this position the turbulence level is very different from the turbulence intensity typical of normal, wind tunnel test section. Some CFD simulations, carried out for the CT3, indicate that the turbulence intensity in this position is around 5%. From these numerical simulations is also possible to estimate the value of μ_t/μ. Finally the nominal design parameters for turbulence are:

- Turbulence intensity TU = 5%

- Turbulence viscosity μ_t/μ=100

These parameters are imposed at domain inlet and outlet. With this set up the adiabatic and the iso heat flux simulations are relaunched and the post process procedure repeated. In figure 2.45 it is presented the mean adiabatic wall temperature around the

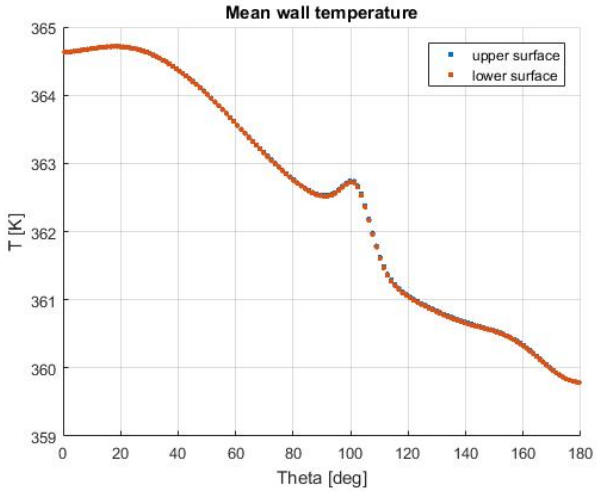

Figure 2.45: Mean adiabatic wall temperature, high turbulent case

two cylinder faces. This distribution is quite different respect to the low turbulence case. Due to the turbulence, at the stagnation point, the temperature does not reach exactly the imposed total temperature (T^o=365 K). Also the sector where the recovery temperature is quite constant is decreasing. With the mean recovery temperature distribution, it is possible to estimate the error due to sensor integral effect at the stagnation point and the error due to the probe angle of attack. As in the low turbulence case the first contribute is very low. Figure 2.46 shows the second contribute in this high turbulence case. The third error contribute is generated by the temperature fluctuations created by the cylinder Von Karman wake that in subsonic flows can influence the forward part of the fluid dynamics field (fig 2.47). In this high turbulence case, the vortex shedding frequency change a little bit. The fundamental frequency in the pressure and temperature spectra grows up from 3580 Hz to 3744 Hz. The positive effect is that, when the

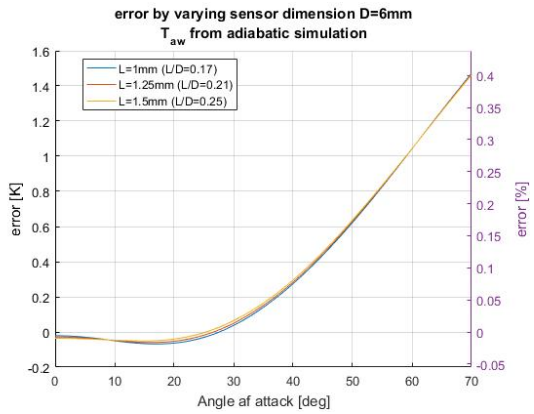

Figure 2.46: Error due to probe angle of attack, high turbulence case

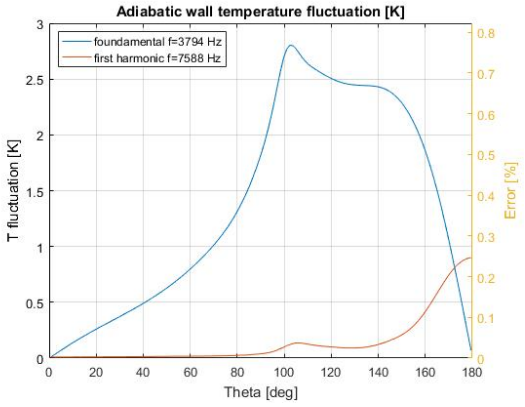

Figure 2.47: Error due to the temperature fluctuations induced by vortex shedding, high turbulence case

turbulence grows up, the wake amplitude is decreasing. This influences the wall temperature fluctuations in the cylinder forward part, that are decreasing too. Finally, in the high turbulence case, the error due to vortex shedding influence is reducing. Particularly if the attack angle is lower than 80 deg this contribute is lower than 1.5 K. Also in this, high turbulence case, it is important to evaluate the Nusselt number and the influence of non linearity in the heat flux phenomena. It is possible to adopt the same procedure implemented in the low turbulence case. Figure 2.48 illustrates the adiabatic

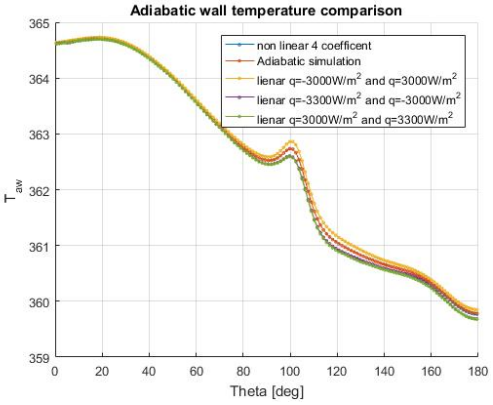

Figure 2.48: Comparison between adiabatic wall temperature computed with different methods, high turbulent case

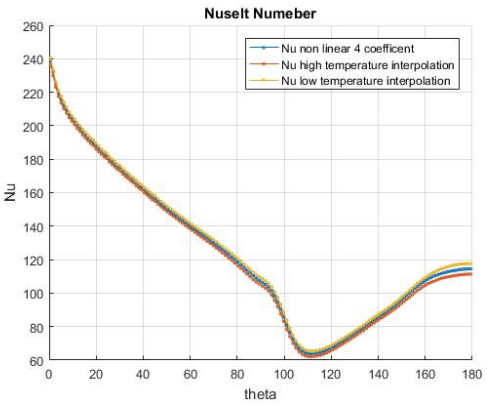

Figure 2.49: Comparison between Nu number computed with different methods, high turbulent case

wall temperature distributions, computed with the five different the methods. Also in

this case the four coefficients interpolation is able to well understand the phenomena and to reproduce the wall temperature computed with the adiabatic simulation. Comparing the results with the low turbulence case it is possible to notice that in this case the differences between the adiabatic wall temperature computed with all the different methods is decreasing; so the non linear heat flux effects seem to decreasing with the turbulence. Using these high turbulence simulations, it is possible to compute the local

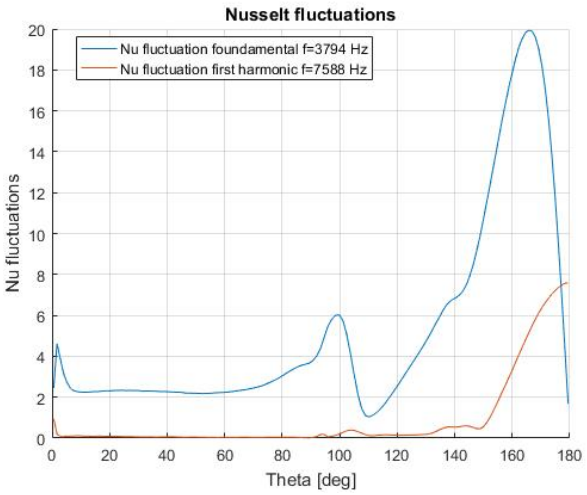

Figure 2.50: Nu fluctuations at high turbulence level

Nusselt number (figure 2.49). The turbulence favourites the heat flux phenomena; this reason explains the increasing in the Nu number respect to the low turbulence case. Also in this case the Nu computed with three different methods presents littler differences. Figure 2.50 shows the Nu amplitudes fluctuation at the two main frequencies. Respect to the low turbulence case the maximum fluctuation amplitude is reducing. For the fundamental vortex shedding frequency, in the forward part of the cylinder, due to the turbulence influence, the amplitude is very low but not zero. It is interesting to analyze the evolution of n and k coefficients (figure 2.51 and 2.52). As predicted by the literature for the flat plate[19], until the separation point, if the turbulence intensity is increasing the n coefficient increase; in the backward part the non linear effect is decreasing with the turbulence. The k coefficient shows that, the turbulence level growing up, reduces the non linear effects of the flow time history.

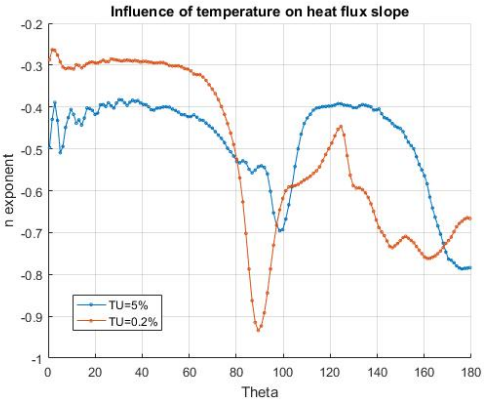

Figure 2.51: Value of n coefficient

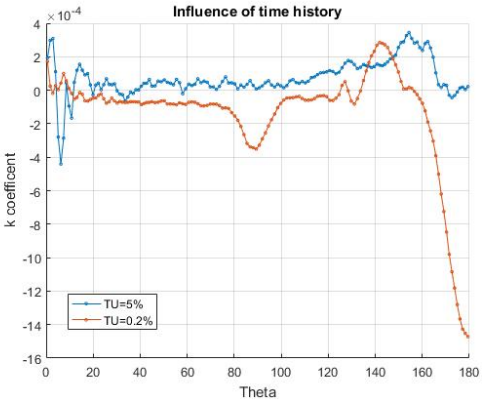

Figure 2.52: Value of k coefficient

Chapter 3

Thermal analysis

The main goal of this chapter is simulating the probe behaviour in real test conditions and developing and algorithm able to manage the experimental post processing data. The chapter contains thermal simulations carried out using as inputs the Nusselt number and the adiabatic wall temperature distribution, obtained with the CFD simulations, in chapter 2. The first section contains some analytical 1D results useful for the probe design. Later the probe 2D model is built, validated and computed. The post process algorithm, based on a 1D conduction model, is tested using the 2D model. Finally, a 3D model of the probe is built and computed in order to evaluate the effects of the 3D conduction. The same kind of analysis is repeated for different probe materials configurations. The last section of this chapter regards some useful considerations useful for the material selection and for the thin film design.

3.1 One dimensional analysis

The final configuration of the probe will be a cylinder with some thin films able to measure substrate wall temperatures. In order to measure the heat flux at different wall temperatures, the probe needs a heater than can warm up the substrate at different levels. The design is made in order to minimize as much as possible the conductive heat flux along the probe z axis. The experimental wall heat flux will be computed with a 1D model, that is unable to evaluate the 3D effect along z; the probe design is carried out in order to preserve the probe symmetry along the z axis. The heater covers all the probe height along the z axis. For the correct estimation of the heat flux at wall, it is required to know the heat flux generated by the heater; the heater heat flux is supposed to be constant during the time test and equally distributed on the heater surface.
In order to ensure this, it is important to understand how the boundary condition oscillations, at the cylinder wall, can penetrate the substrate and if they can reach the heater. A simple 1D model is solved; the heat flux equation is:

$$\frac{1}{\alpha}\frac{\partial T}{\partial t} - \frac{\partial T^2}{\partial^2 x} = 0 \tag{3.1}$$

Material	ρ $\left[\frac{Kg}{m^3}\right]$	C_p $\left[\frac{J}{Kg \cdot K}\right]$	k $\left[\frac{W}{m \cdot K}\right]$	μ at f=2 Hz $[m]$
MACOR	2520	752	1.672	$3.74 \cdot 10^{-4}$
KAPTON	1420	1090	0.120	$1.11 \cdot 10^{-4}$

Table 3.1: Material thermal proprieties

where α is

$$\alpha = \frac{k}{\rho c_p} \tag{3.2}$$

A semi infinite domain is selected and a oscillating heat flux is imposed on one boundary:

$$Q(t) = Q_0 \cdot (1 + cos(\omega t))/2 \tag{3.3}$$

The non stationary part of the solution is [28]

$$T(x,t) = \frac{Q_0}{2\epsilon\sqrt{\omega}} e^{-x/\mu} cos\left(\frac{x}{\mu} - \omega t + \frac{\pi}{4}\right) \tag{3.4}$$

where

$$\mu = \sqrt{\frac{k}{\rho c_p \pi f}} \tag{3.5}$$

and

$$\epsilon = \sqrt{k \rho c_p} \tag{3.6}$$

The equation is parabolic so, the boundary condition, is heard instantaneously in the entire domain. It is important to understand how much the material can damp the boundary condition oscillations. The μ parameter, called depth of penetration, represents the length in which the temperature fluctuations are reduced of an exponential factor. The material and the considered frequency influences the μ factor. If the frequency grow up, the temperature oscillations are dumped more. Table 3.1 summarizes the thermal proprieties of 2 different polymers, MACOR and KAPTON[7]. The μ factor is computed at frequency of 2 Hz because the CT3 test will last almost 0.5 s; 2 Hz is the highest frequency of interest to guarantee the heat flux during the test does not influence the field on the heater surface. For both the materials μ is an order of magnitude lower than the probe diameter; the temperature fluctuations will reach the heater really dumped and we can consider the heat flux on the heater constant in space and in time.

3.2 2D probe model

For the 2D case does not exist an analytical solution. The 2D heat flux problem will be solved using a numerical procedure based on finite elements approach. The solution is obtained using the heat transfer package of Comsol Multiphysics. A crucial point is to build a mesh, able to approximate correctly the solution but, at the same time, able to limit the computation cost of non stationary calculations. In case of particular 2D

geometry, with particular boundary conditions it is possible to find the stationary, analytical solution. This solution is useful to validate the Comsol mesh level of refinement. This simplified geometry, presents a MACOR cylinder with a diameter of 6 mm; inside in the center, a heater with a diameter of 2 mm. On the heater surface the boundary condition is constant heat flux of Q=13850 W/m^2. On the probe external surface, in this test case, we imposed the adiabatic wall temperature coming from the high turbulence CFD analysis (cap. 2). The steady state equation is:

$$\nabla^2 T = 0 \tag{3.7}$$

using cylindrical coordinates became:

$$\frac{1}{r}\frac{\partial T}{\partial r} + \frac{\partial^2 T}{\partial r_2} + \frac{1}{r^2}\frac{\partial^2 T}{\partial \theta^2} = 0 \tag{3.8}$$

with, as a boundary conditions:

$$\begin{cases} T = T_{aw} \text{ on the external surface} \\ \\ k\frac{\partial T}{\partial n} = Q \text{ on the internal heater surface} \end{cases} \tag{3.9}$$

the general solution is:

$$T = A_0 + B_0 + \sum_1^n \left[A_n r^n + B_n r^{-n}\right] cos(n\theta) \tag{3.10}$$

In order to implement the boundary condition it is necessary to expand the wall temperature distribution in cosine series.

$$T_w = \sum_0^\infty a_n cos(n\theta) \tag{3.11}$$

The series coefficients could be find as:

$$a_0 = \frac{1}{\pi}\int_0^\pi T_w(\theta)\, d\theta \tag{3.12}$$

and

$$a_n = \frac{2}{\pi}\int_0^\pi T_w(\theta)\, cos(n\theta) d\theta \tag{3.13}$$

in our case a 50 harmonics approximation is implemented. Using this expansion it is possible to calculate the coefficients A_n and B_n.

$$B_0 = -\frac{Q}{2\pi k} \tag{3.14}$$

$$A_0 = a_0 - B_0 log(r_{probe}) \tag{3.15}$$

$$A_n = a_n \frac{r_{probe}^n}{r_{probe}^{2n} + r_{heater}^{2n}} \tag{3.16}$$

$$B_n = A_n \cdot r_{heater}^{2n} \tag{3.17}$$

Knowing these coefficients the solution is completely defined. The same case is solved with Comsol using the "finer" level of refinement; the mesh contain 1826 elements. The steady solution is computed and compared with the analytical one. The maximum error between the two solutions, is very low (less than 0.006 K); the mesh refinement level is validated. In the real probe, in order to limit the influence of temperature fluctuations on the heater surface, the heater is positioned not in the probe center but 1 mm backward. This second geometry is studied using a mesh with the same level of refinement. The initial goal is to understand if the 2D effects can influence the penetration of wall boundary condition. A time dependent simulation is launched with adiabatic condition on the heater and fluctuating temperature conditions on the probe surface. The fluctuation contains different frequencies:

$$T = 300 + A \cdot sin(2\pi \cdot 1 \cdot t) + A \cdot sin(2\pi \cdot 2 \cdot t) + A \cdot sin(2\pi \cdot 10 \cdot t) \tag{3.18}$$

Figure 3.1 illustrates the temperature fluctuation amplitudes, at different distances from the probe surface, extracted on the probe axis of symmetry. On the probe surface

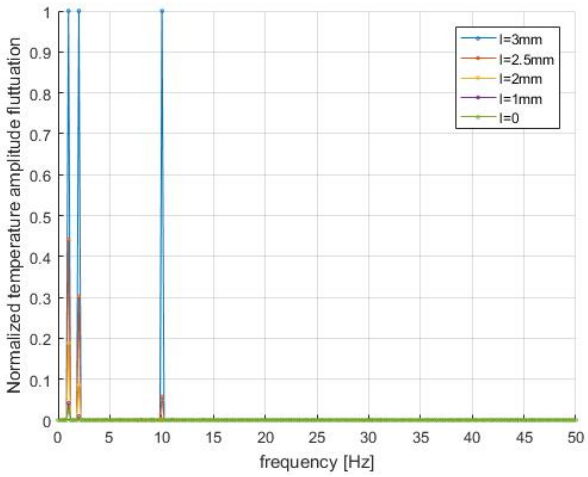

Figure 3.1: Spectra at different surface distances

(l=3mm) all the frequencies (1, 2 and 10 Hz) have the same amplitude. Entering in the material the lowest frequencies are less dumped. On the heater surface (l=0) all the fluctuations are very low, in particular the fluctuations at 2Hz (test time 0.5 s) could be neglected. The final selected 2D geometry is a circular 6 mm diameter probe with a 2 mm diameter heater. The heater is positioned not in the probe center but 1 mm backward. In order to increase the accuracy in the boundary heat flux estimation the domain limits are meshed with quadrangular stretched elements. In the normal direction

6 elements are positioned with a total thickness of $1.02 \cdot 10^{-4} m$. The selected grow rate is 1.3. Figure 3.2 shows the final 2D build mesh containing 2438 elements. The thin

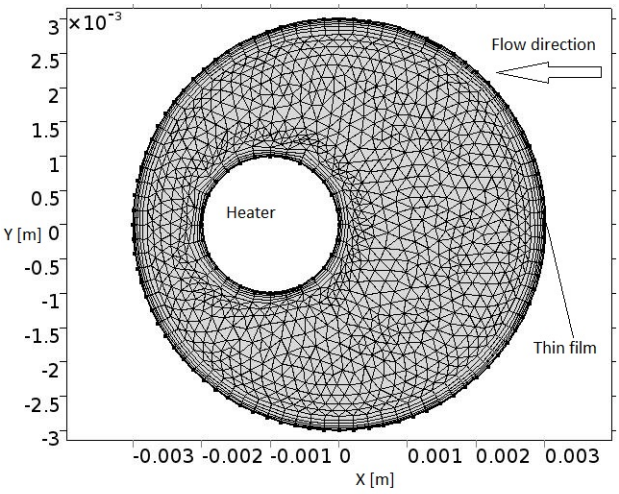

Figure 3.2: Computed mesh for the 2D study

film amplitude in this case is 1.5 mm and the film is placed centred respect to the probe stagnation point. Now the boundary conditions has to be defined; on the heater surface a Neuman condition is selected.

$$\frac{\partial T}{\partial n} = -\frac{1}{k} Q_{heater} \tag{3.19}$$

on the probe external surface a Robin boundary condition is imposed

$$Q = h(T_{aw} - T) \tag{3.20}$$

and on the thin film surface:

$$Q = h(T_{aw} - T) + Q_{thinfilm} \tag{3.21}$$

The heat flux generated with the thin film is 200 W/m^2. This is choose just as a first approximation [7]; in the final section of this chapter an accurate study for thin film will be carried out. Using this set-up different experiments varying the heater condition are carried out. Always the first point is to simulate the initial condition. At the experiment beginning the probe is positioned in the facility, the heater and the thin films are switched on; in the facility there is the ambient temperature (T=293 K), the pressure is very low and the convective coefficient is very low too(h=$5W/(Km^2)$). Figure 3.3 illustrates the initial temperature field, with the heater switched on at $Q_{heater} = 1200W/m^2$. When the test begins a septum is opened and the pressurized air enters in the facility test section and skims the probe. When the system is at full speed, the convective heat flux coefficient (h) and the adiabatic wall temperature (T_{aw}) reach the values (θ depending)

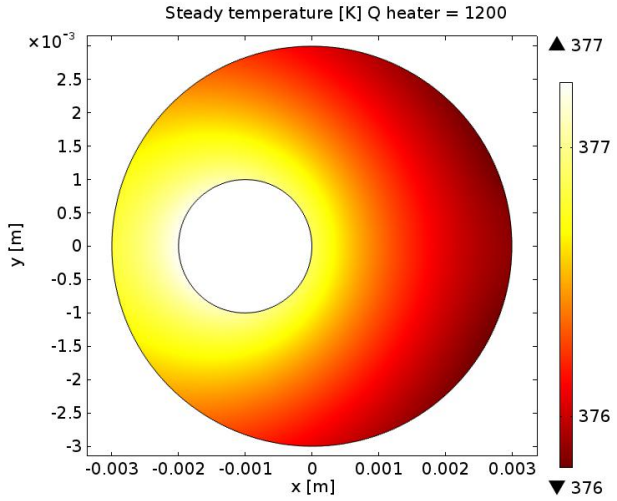

Figure 3.3: Probe initial temperature field $Q_{heater} = 1200W/m^2$

computed with CFD analysis at high turbulence (cap. 2). During the transition for the h coefficient a smoothed, 0.05 seconds ramp is supposed. The adiabatic wall temperature case is quite different. When the air starts to flow a compression wake is generated, this create a temperature overshoot. At the end of the test, the temperature remain constant but the velocity returns to be very low, therefore the h coefficient return at h=$5W/(Km^2)$. Figures 3.4 and 3.5 shows the average, h and T_{aw} time histories, on the sensor. In order to reach a good resolution during the the convection step, a 0.001 s time step is used. The simulations are launched for different heater conditions:

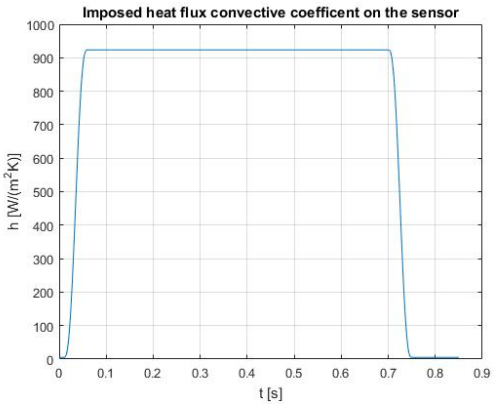

Figure 3.4: Heat flux coefficient time history on the sensor

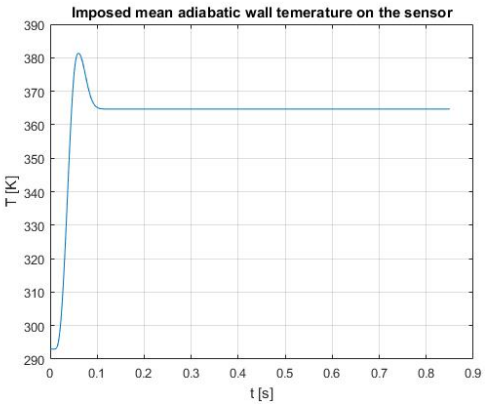

Figure 3.5: Adiabatic wall temperature time history on the sensor

- Heater switched off (Q=0)

- Heater with Q=800 W/m^2
- Heater with Q=1000 W/m^2
- Heater with Q=1200 W/m^2
- Heater with Q=1400 W/m^2

The different power conditions are chosen in order to simulate, some cases where the probe is hot and the flow is cooling and some cases where the probe is cold and the flow is heating. Figure 3.6 shows the mean temperature time histories on the thin film. When

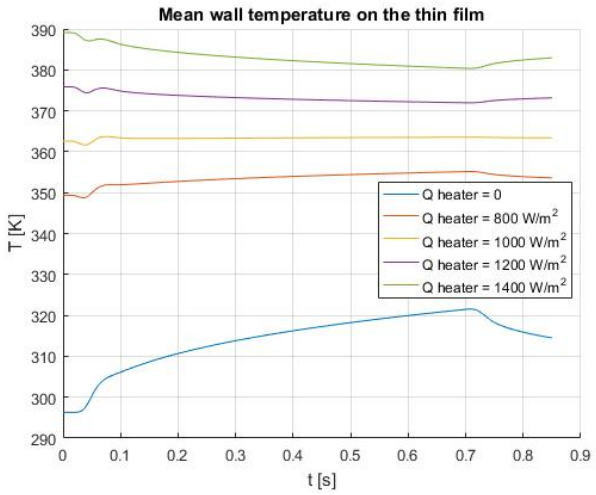

Figure 3.6: Temperature time history on the sensor

the heater is switched off, the probe temperature is low and, when the flow arrives, it starts to heat the sensor. When the heater power is growing, gradually the initial temperature on the sensor is increasing, at the highest power condition, the sensor is hotter than the flow, so when the flow arrives it starts to cool the sensor. In figure 3.8 it is showed the mean convective heat flux history on the sensor, in this case a positive heat flux means an incoming flux. The convective heat flux is computed as:

$$Q_{conv} = Q_{conduction} - Q_{thinfilm} \tag{3.22}$$

When the heater power is low, the probe is cold and during the test the heat flux is entering in the probe (positive). When the heater power increase, the probe temperature is increasing too, so the heat flux on the sensor is decreasing and it can became negative (the probe heats the flow). It is important to prove the model linearity in the entire operative field. We select some time steps and plot the sensor temperature and heat flux on a temperature/convective heat flux graph (figure 3.8). In the same figure are added the adiabatic cases with null heat flux and adiabatic wall temperature; the model linearity is verified. Using this model a h coefficient and an adiabatic wall temperature

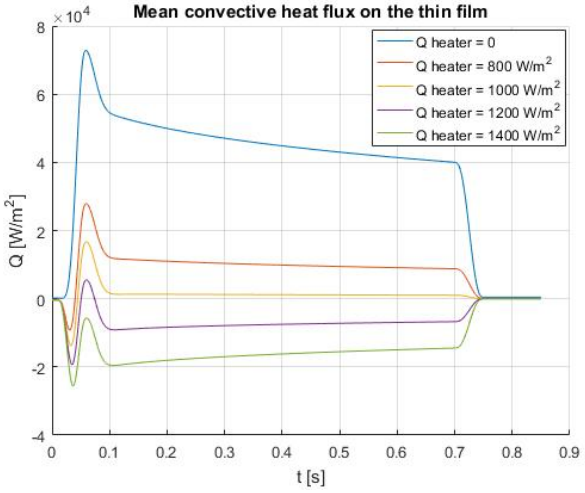

Figure 3.7: Heat flux time history on the sensor

are imposed on the probe wall and on the sensor, launching the calculations at different heater powers, it is possible to obtain the convective heat flux on the sensor at different probe temperatures. As expected, using linear interpolation, it is possible to re find the imposed T_{aw} and heat flux coefficient h with very good accuracy.

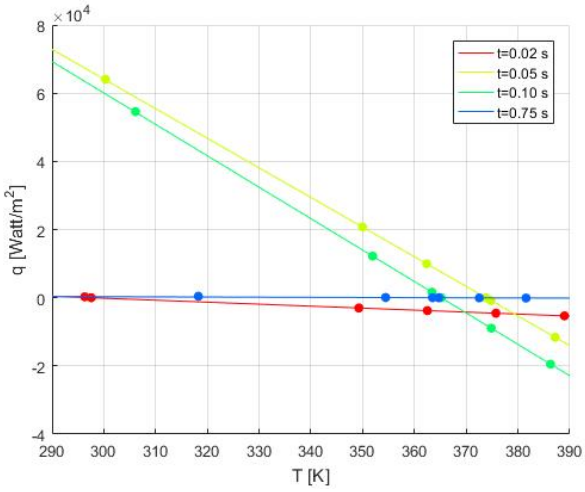

Figure 3.8: Example of heat flux temperature interpolation

3.3 1D model for the heat flux calculation

This section contains the description and validation of the post processing algorithm. The experimental set-up permits to measure the electrical quantities on the thin film; these are used to define the sensor temperature. It is required to develop a model able to estimate, starting from the wall temperature, the mean heat flux on the sensor. The idea is to use a 1D model. The simpler 1D model consists in a 1D bar model with, a boundary conditions, on the right side the thin film temperature and on the left side the adiabatic condition. In this case the conduction equation (eq. 3.1) has an analytical solution [31]. It is possible to find the heat flux on the sensor as:

$$Q_w = \frac{T_w(t) - T_w(0)}{2\sqrt{t}} \sqrt{\pi \rho c k} \tag{3.23}$$

The second idea is to use a 1D model with different boundary conditions. In this case the heater heat flux is imposed on one domain side and the thin film temperature on the other. The initial solution is founded solving the stationary 1D heat flux equation imposing the initial thin film temperature. In this case the initial temperature distribution in the domain will be linear with the slope imposed by the heater heat flux. Finally a new post process corrected method is developed and numerically tested. The complete heat flux equation is:

$$\frac{1}{\alpha}\frac{\partial T}{\partial t} - \nabla^2 T = 0 \tag{3.24}$$

Using cylindrical system of coordinates it is possible to expand the equation as:

$$\frac{1}{\alpha}\frac{\partial T}{\partial t} - \frac{1}{r}\frac{\partial T}{\partial r} - \frac{\partial^2 T}{\partial r^2} - \frac{1}{r^2}\frac{\partial T^2}{\partial \theta^2} = 0 \tag{3.25}$$

Supposing the system with θ symmetry the last term in the equation is equal to zero and the problem become mono dimensional, solvable using the heater heat flux and the thin film temperature as boundary conditions. In this case the initial condition is founded by solving the stationary case of the equation with the initial thin film temperature. For the correct solution evaluation it is necessary to solve the equation between r_{heater} and $r_{heater} + r_{probe}$; the solution is not linear but the general steady solution is:

$$T = A + Blog\,(r) \tag{3.26}$$

The A and B coefficients come the boundary conditions.

$$A = T_{w0} + \frac{Q_{heater} r_{heater}}{k} log(r_{ext}) \tag{3.27}$$

and

$$B = \frac{Q_{heater} r_{heater}}{k} \tag{3.28}$$

Figure 3.9 shows the comparison between the three initial 1D conditions and the 2D initial condition along the axis $\Theta = 0$. The comparison is between an adiabatic condition

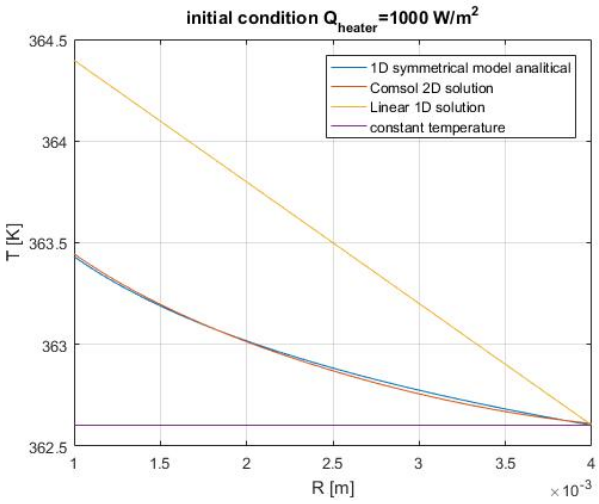

Figure 3.9: Comparison with different initial solutions

on the left boundary, which produces a uniform temperature, a linear distribution, obtained by the 1D model, and finally the logarithmic temperature distribution (eq.3.26) of the 1D axis symmetrical model. This last model approximates very well the steady 2D solution. The different 1D models are tested using the thin film temperature time history extracted from the 2D simulations. Figure 3.10 shows the time history of the computed heat flux when $Q_{heater} = 1200W/m^2$. The 2D solution allows to estimate the

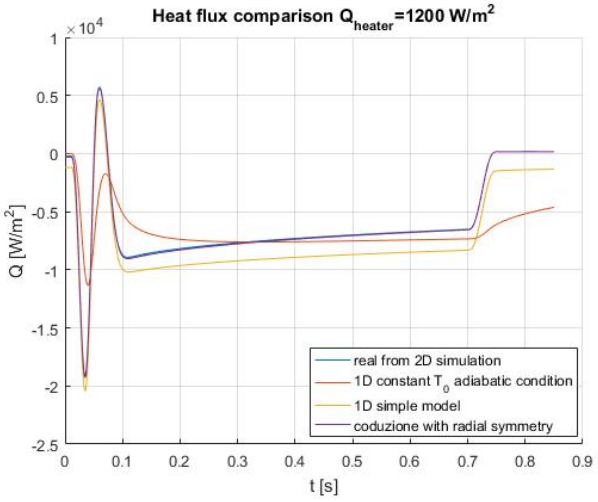

Figure 3.10: Comparison heat flux computed with different models $Q_{heater} = 1200W/m^2$

error of the one-dimensional model. It is possible to estimate the 1D model error as:

$$error = Q_{1Dmodel} - Q_{2D} \tag{3.29}$$

Figure 3.11 illustrates the errors of the 1D model and 1D axisymmetric models. The superiority of the axisymmetric model is clearly evident. Finally it is possible, with the

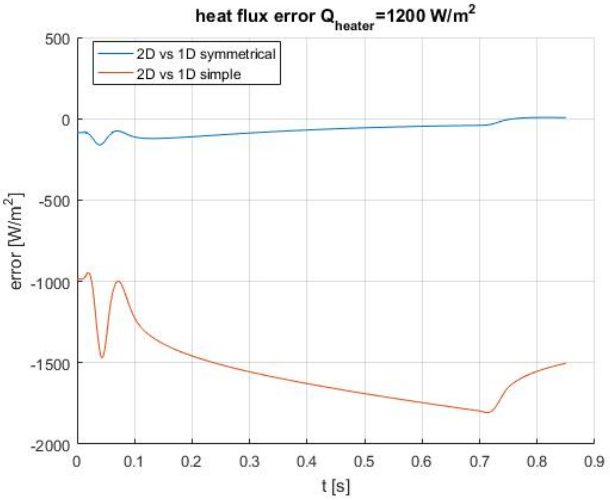

Figure 3.11: Error between different 1D models $Q_{heater} = 1200 W/m^2$

computed heat fluxes, to calculate the gas temperature and compare the results with the imposed adiabatic wall temperature. A linear interpolation is used:

$$T_{aw} = T_1 + Q_1 \frac{T_2 - T_1}{Q_1 - Q_2} \tag{3.30}$$

Figure 3.12 shows the results, obtained with the two last models. Both the models are

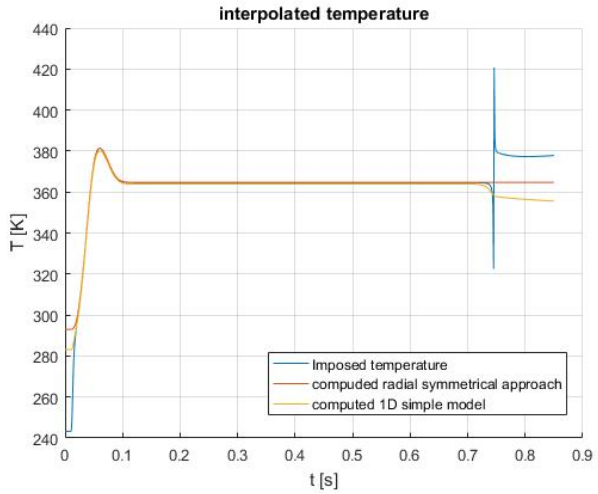

Figure 3.12: Comparison between imposed and interloped temperature

able to estimate the imposed adiabatic wall temperature. At the test begin and end, the

error increase a lot; this because in these cases the heat flux coefficient h is very low and so, the wall heat flux is very low too. At these times the error made by the 1D models in the heat flux estimation, is higher than the real heat flux value. This is not a real problem in fact the probe has to work in the measurement region (central part of the test) when the h coefficient and the heat flux are high. Figure 3.13 illustrates a comparison between the error make by the two different methods, in the adiabatic wall temperature reconstruction, in the central region of the test. With the 1D model corrected with radial

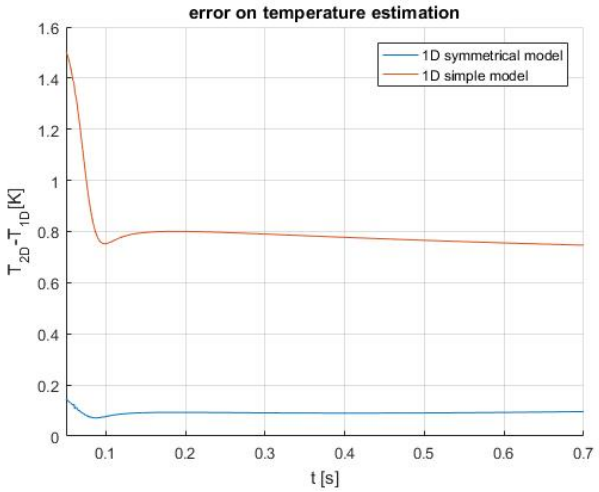

Figure 3.13: Error on the reconstruction of the adiabatic wall temperatureT_{aw}

symmetry it is possible to reduce the error of almost one order of magnitude, respect to the normal 1D approach. Finally, comparing the imposed adiabatic wall temperature with the T_{aw} obtained processing the wall temperature with the 1D corrected model, the error seems to be less than 0.1 K.

3.4 3D model

Finally a 3D complete probe model is built and computed. Figure 3.14 contains the model geometry ,11 thin films are positioned on the probe; the thin films are 1.5mm wide and 1.0mm high. The thin films distance of 2mm is chosen in order to limiting their mutual interference. The total probe height is 40mm. The upper part presents a 5mm support where the probe will be fixed. Inside the probe a 34mm height heater is placed, starting from 1mm to the probe lower surface and arriving until the probe support; the material chosen for the probe is MACOR. The boundary conditions are quite similar to the 2D case. During the tests time the heater and the thin films are switched on; the heater power is variable depending from the test, the thin films heat flux is set at 200 W/m^2. The support surface, supposing the presence of an insulating layer, is modelled with an adiabatic wall condition. All the surfaces, exposed at the flow at the test beginning are modeled with low convection condition (h = 5 W/m^{2}K and

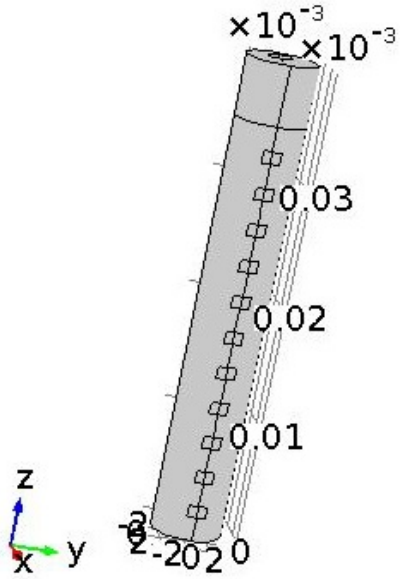

Figure 3.14: 3D model geometry

T_{aw}=T_{amb}=293 K). The non stationary simulations are initialized with the temperature field obtained with the stationary, pre-test solutions. During the transient simulations on the probe lateral surface and on the thin films, the boundary conditions time histories are the same used in the 2D case. On the probe basis the adiabatic wall temperature is the same respect to the lateral surface. For the heat flux coefficient h, the probe base is associated at a flat plate. It is possible to compute the Nusselt number as [2]:

$$\overline{Nu_L} = \left(0.037 Re_L^{4/5} - 871\right) Pr^{1/3} \tag{3.31}$$

The support lateral surface remains adiabatic for all the test duration, and also the probe upper surface remain exposed at atmospheric and low Nusselt condition for all the test duration. The built 3D mesh use around 50000 elements, in order to limit the computational cost the time step is increased at 0.0025 s and the simulation time is reduced at 0.5s, sufficient to simulate all the probe measurement region. The same procedure employed for the 2D simulation is used in this case. The 3D simulation is launched with Q_{heater} equal to 1000 W/m^2 and 1200W/m^2. The wall temperature histories averaged on the thin films are extracted; these temperatures are processed with the 1D radial symmetry code. The heat flux histories are obtained at different wall temperatures and, using these, with a linear interpolation, the adiabatic wall temperature is computed. As in the 2D model the temperature estimation is bad when the heat flux is very low (test beginnings).Figure 3.15 compares the computed temperature time histories, in the probe measurement region, for the different thin films, with the imposed adiabatic wall temperature. The error between the imposed and the measured temperature is around

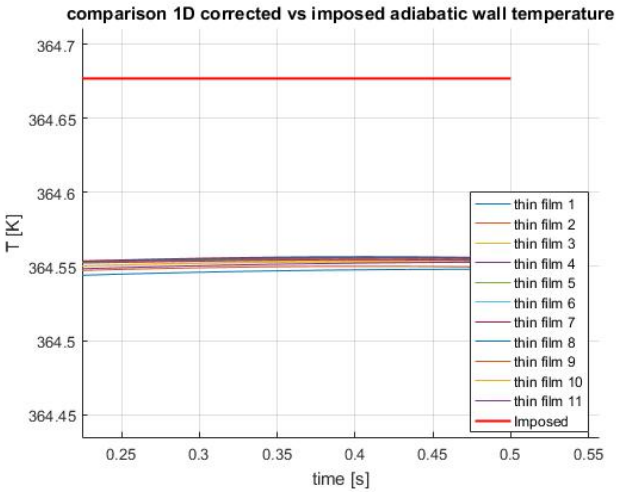

Figure 3.15: Adiabatic wall temperature time history in the measurement region

0.1 K; also the temperature difference between the 11 different thin films is very low; the 3D conduction effects seem to have very low influence on the temperature measurement. It is important to understand if the error due to the 3D conduction is really negligible, if not a 3D correction is necessary. The more critical thin film is the first one near the probe base. Due to the convection on the base, in this zone, the z temperature gradient is more accentuated. In order to estimate this effect, the error between the temperature measured with the thin film 1 and the imposed temperature, is compared with the error between the temperature coming form the post process of the 2D case and the imposed temperature.(figure 3.13). Figure 3.16 illustrates comparison between the errors. The

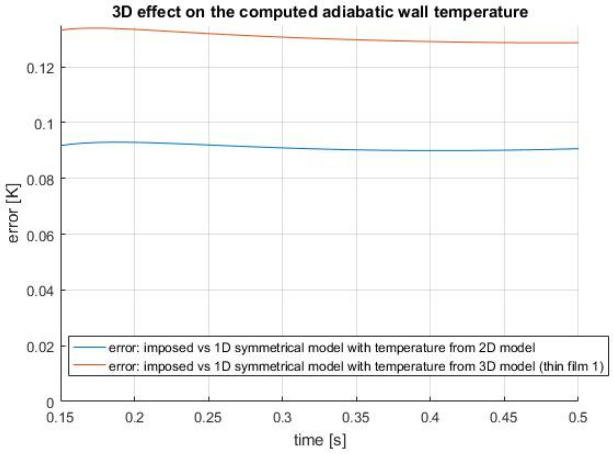

Figure 3.16: Comparison between 2D and 3D error in the measurement region

difference between the errors is very low (about 0.03 K), the 3D conduction effects can

be neglected and it is useless to develop a 3D conduction correction.

3.5 Double layer solution

It exists two different thin film manufacturing techniques. The first one consists in painting the thin film directly on the substrate. The different thin film resistances are obtained by overlapping different metal layers. In this case the minimum sensor dimension depends from the technician ability but could be around 1×1.5 mm. The advantages are: this process is homemade in VKI, these thin films are more robust and there are not broken risks in thin film and in the electrical connections, due to the probe substrate curvature. The other technique is based on the photo lithography production method. The thin film material is placed on a polymer substrate (KAPTON in our case) by an external company; later the KAPTON layer ($200\mu m$) is glued on the MACOR substrate. In this case the disadvantages are the complexity due to the bonding resistance also at high temperature, the risk of bubbles creation between the two layers and the necessity to simulate, also with the 1D model, the material interface.The main advantage is the independence from the technician ability and availability. In this case the sensor dimensions depends principally from the required sensor power. Finally, for the prototipe, the second option is chosen. It is required to build a 2D model able to simulate this manufacturing solution. The KAPTON thermal proprieties are summarized in table 3.1. The geometry is the same used for the single layer case, a $200\mu m$ KAPTON layer is added around the 6 mm diameter MACOR substrate. The MACOR mesh is built as in the 2D single layer case. The KAPTON layer is meshed with a mapped mesh with 5 elements in the normal direction [7]. The final 2D mesh is presented in figure 3.17. The boundary conditions time histories are the same using

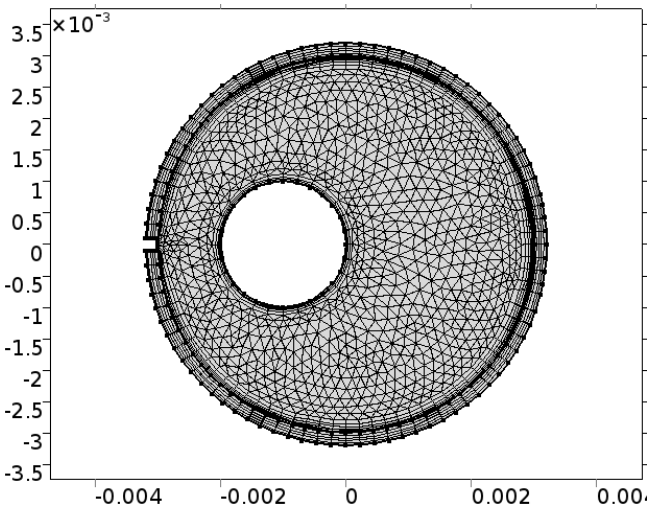

Figure 3.17: Double layer mesh

in the single layer case. In this case the simulations are launched with Q_{heater} equal

to 1200 W/m^2 and 1000 W/m^2.Figure 3.18 shows the initial stationary solution with Q_{heater} = 1200 W/m^2. In figure 3.19 there are showed the initial solutions, for two

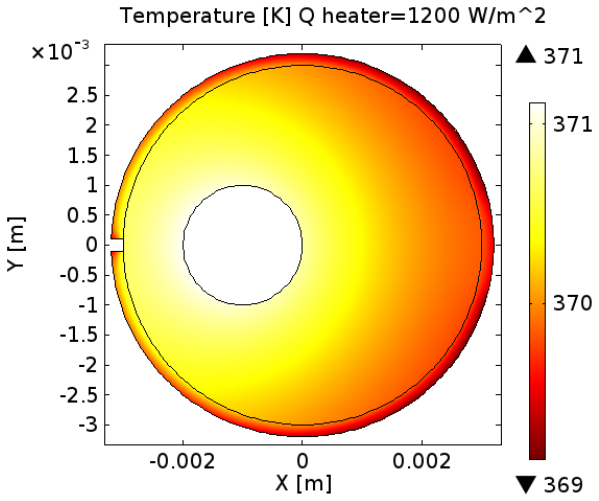

Figure 3.18: Initial double layer solution with $Q_{heater} = 1200 W/m^2$

heater powers, plotted at $\theta = 0$. It interesting to notice that the solutions are not a C1 functions at the material interface point. In this point the material thermal conductivity (k) is varying, so the temperature r derivate is not continuous. The goal in this case, is

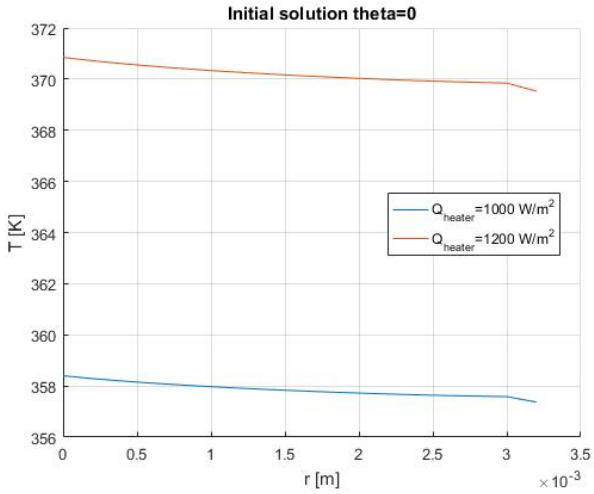

Figure 3.19: Initial solutions $\theta = 0$

to repeat the single layer analysis in order to validate, also using this configuration, the post process routine. Supposing Q_{heater} equal to 1000 and 1200 W/m^2, starting from steady low convection conditions, and imposing the T_{aw} and h time histories, presented for the single layer case (figure 3.5 and 3.4), the transient simulations are launched and

the thin films time histories are obtained. In order to reproduce the experimental post process procedure a 1D model is built. In this case the mesh building procedure is quite critical. The KAPTON thermal diffusivity is more than one order of magnitude lower than the MACOR one; the greatest part of the thermal gradient is located in the KAPTON 0.2 mm layer. The 1D mesh has to be able to reproduce these different gradients, limiting at the same time the number of cells. The KAPTON layer is divided in 50 cells, for the MACOR substrate 100 cells are used. In order to maintain the continuity in the cells dimension at the material interface, the length ratio between the first and the last MACOR cell is fixed at 10. Finally the computed 2D temperature history is fixed on the domain right side, and the heater heat flux on the other one. The 2D correction, explained for the single layer model, is adopted and the wall heat flux for the two different heater conditions is computed. The wall temperatures, and the respective wall heat flux time histories, are available. Using a linear interpolation, the heal flux coefficient h and the adiabatic wall temperature are calculated; the results are quite similar to the single layer case. With the 1D corrected model it is possible to well recognise the adiabatic wall temperature when the heat flux coefficient is quite high. At the test beginning, h is very low and the error in heat flux estimation is higher than the real heat flux so the error on the adiabatic wall temperature is very high. Figure 3.20 and 3.21 presents the computed T_{aw} time history and the error time history, between the temperature imposed in the 2D model and the computed one.

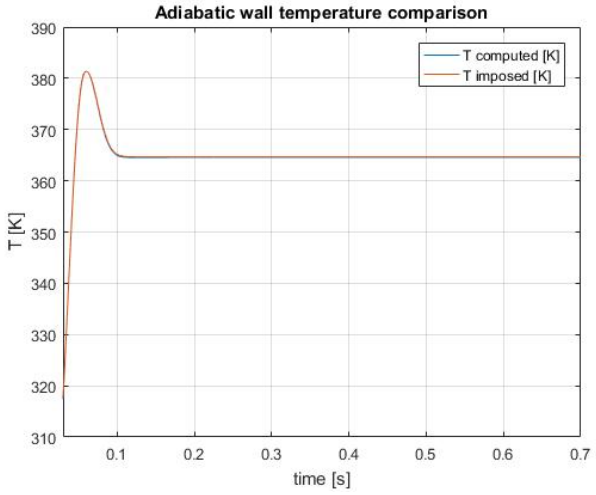

Figure 3.20: Computed and imposed T_{aw} on the sensor

3.6 Thin film design

This section contains some considerations useful for the probe materials selection and the thin films design in the double layer case. The first point is to well select the probe substrate materials. The goal is to maximise the thin film dynamic response. The thin

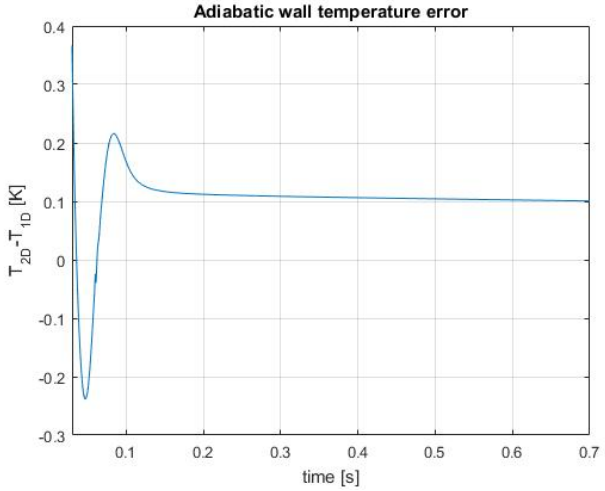

Figure 3.21: Error between computed and imposed T_{aw} on the sensor

Material	ρ $\left[\frac{Kg}{m^3}\right]$	c_p $\left[\frac{J}{Kg \cdot K}\right]$	k $\left[\frac{W}{m \cdot K}\right]$	$\sqrt{\rho c_p k}$ $\left[\frac{J}{m^2 k s^{0.5}}\right]$
MACOR	2520	752	1.672	1779
KAPTON	1420	1090	0.120	431.0
Quartz	2200	670	1.40	1436

Table 3.2: Materials thermal product

film is glued on the substrate surface that, due to conductive heat flux, is changing his temperature. The limit in the frequency response of the system is due to the ability of the thin film to adapt at the substrate wall temperature. Fixing the in coming heat flux, it is important to minimize the changing in the wall temperature. With the photo lithography technique it is very difficult to build the thin film directly on the probe substrate. The sensor is built on a KAPTON substrate, later glued on the probe. For the double layer configuration the conductive heat flux, in case of adiabatic condition on one domain side is[9]:

$$q = (T_w(t) - T_i) \cdot \left(\frac{2\sqrt{t - t_0}}{\sqrt{\pi}\sqrt{\rho_2 c_2 k_2}} + \frac{l}{k_1} \left(1 - \frac{\rho_1 c_1 k_1}{\rho_2 c_2 k_2} \right) \right)^{-1} \tag{3.32}$$

Where the material one is the first one, outside of the probe with a thickness l. In our case the KAPTON thickness is around 0.2 mm, so the last term in the previous equation could be, at first approximation, neglected. The equation for the conductive heat flux become equal to equation 3.23 used for the single layer case. In order to minimize the changing in the wall temperature, the material selected for the probe substrate, has to maximize the thermal product ($\sqrt{\rho C_p k}$). Some possible materials are list in table 3.3. Finally the MACOR is selected. For the thin film a serpentine shape is selected; this choice permits to maximize the sensor performances in therms of spatial resolution and,

Material	$\rho_0\ 10^8\,[\Omega m]$	$\alpha_0\ [1/K]$	$\rho_0\alpha_0\ 10^8\,[\Omega m/K]$
Nickel	6.84	0.00690	0.0472
Platinum	10.6	0.00392	0.0416
Chromium	12.9	0.00300	0.0387

Table 3.3: Thin film materials proprieties

Width W [mm]	Length L [mm]	Thickness h [nm]	Wire width w [mm]	R_0 [Ω]
0.87	0.8	200	0.05	49.1

Table 3.4: Thin film proprieties

at the same time, sensor resistance. For the complete thin film design it is necessary to define the thin film material and the thin film geometry; in particular, the total surface covered by the thin film in length and width (L and W), the thin film thickness t and the coils number and width. The thin film resistance is a temperature function so, using the resistance measurements, it is possible to estimate the thin film temperature that is assumed equal to the substrate wall temperature. The resistance of a thin film with heigh h, length l and with w can be approximated as[4]:

$$R(T) = \frac{\rho_0 l}{hw}\left[1 + \alpha_0\left(T - T_0\right)\right] \tag{3.33}$$

When a constant current is used on the sensor, the measured potential difference is

$$E - E_0 = i\left(R - R_0\right) = iR_0\alpha_0\left[T - T_0\right] = i\frac{l\rho_0}{hw}\alpha_0\left(T - T_0\right) \tag{3.34}$$

The thin film material is chosen in order to maximize the thin film thermal sensibility, so the the product $\rho_0 \cdot \alpha_0$ has to be as high as possible. In table 3.3 some materials are analysed; finally a Nickel thin film is chosen.
The principal goal in this design analysis is to increase the signal to noise level. Due to the joule effect the result of the current in the thin film is an electrical heat flux. During the test the thin film temperature is changing, so the resistance and the electrical heat flux are changing. It is important to keep the variation of the dissipative heat flux (Δq_{diss}) negligible, respect to the measured conductive heat flux[15].

$$\frac{\Delta q_{diss}}{q_{cond}} < \epsilon \tag{3.35}$$

The Δq_{diss} could be expressed as:

$$\Delta q_{diss} = \frac{i^2\left(R - R_0\right)}{WL} = \frac{i^2 R_0\left(T - T_0\right)\alpha_0}{LW} \tag{3.36}$$

The conduction heat flux during the test is estimated with the equation 3.32. Fixing in equation 3.35 $\epsilon = 1.5\%$ it is possible to find the thin film resistance $R_0 = 49.1\Omega$. In our

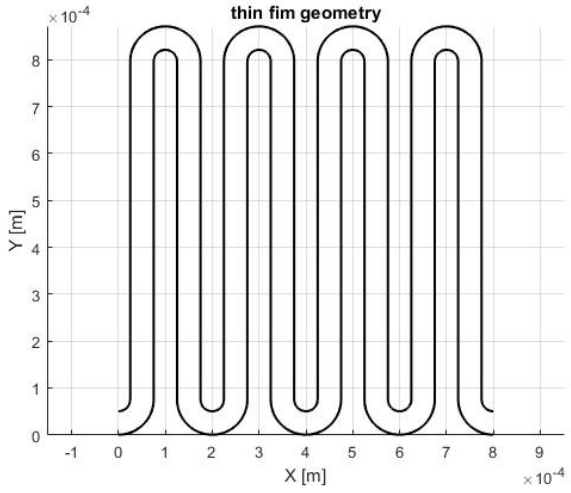

Figure 3.22: Designed thin film

case the selected courrent, crossing the thin film sensor, is equal to 5mA; this value is quite low, but permits to reduce the 2D lateral conduction effects. Typical values of thin film wire thickness (h) and with (w) are h=200nm and w=0.05mm chosen in order to maximize the frequency response and the thin film robustness[7]. With this assumption it is possible to evaluate the thin thin film wire length and the number of coils required to reach the desired resistance. The total thin film area ($L \times W$) is adapted in order to reach the desired length with an entire number of coils. Figure 3.22 presents the final designed thin film. Table 3.4 summarizes the final thin film proprieties.

Chapter 4

Experimental analysis

This chapter describes of the first experiential tests carried out with the probe. The typical CT3, plane 3 flow conditions are reproduced with a jet and the probe behaviour is tested. The first point is to create a jet with a stable total temperature measured with a thermocouple. Secondly point we made many measurements with the probe in the constant temperature jet. In this case the principal goals are: investigating about the flow reproducibility during different tests; validating the linearity in the heat transfer phenomena at different wall temperatures; measuring with a linear regression, the flow temperature and the Nusselt number at the stagnation point in order to validate the designed probe measurements.

4.1 Probe construction and calibration

The VKI technician built a first prototype of the probe. In order to reduce the manufacturing costs and times the mounted sensor is the double thin film sensor designed by A. J. Carvalho [7]. This sensor presents two thin films with a resistance of 100 Ω and 50 Ω respectively. Each thin film is $0.7 \cdot 1.5mm$ wide and 200 nm thick. In our case, in order to reproduce the single thin film behaviour, only the lowest resistance will be used. The sensor longest side is placed along the z axis of the probe cylinder. With this solution we can avoid all the breakage problems, had in Carvalho's work, at the interface between the nickel resistance and the gold connections, due to the substrate curvature. The sensor is deposed on KAPTON layer of 0.2mm later glued, by the VKI technician, on the probe substrate. The substrate consists in a MACOR cylinder of 4.6 mm of diameter trilled in the center for hosting the 1.7mm diameter and 50mm length heater. The heater is home made at VKI and consists in a wire (resistance of $6,5 ft\Omega$ and section diameter of 0,25mm), coiled around a MACOR cylinder in 50 loops, in order to achieve a resistance of approximately 5.5Ω. Figure 4.2 shows a photo of the final built probe prototype. When the manufacturing process finished the probe was put in the oven and 7 thermal cycles from ambient temperature to 85 degrees were carried out. The aim of this process is to reduce process the thin film broken risks during the tests and avoid, as much as possible, the mechanical tensions in the probe materials that can influence

Figure 4.1: Sensor of the probe prototype

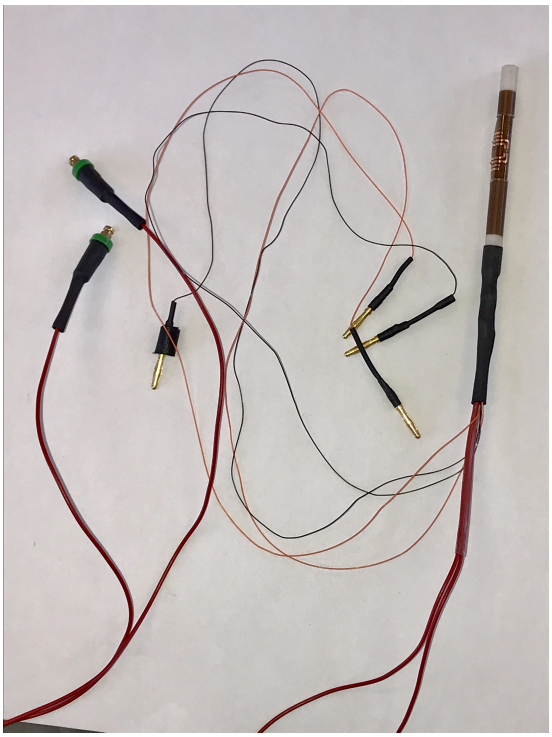

Figure 4.2: Probe prototype

the calibration law. The temperature increased by steps of 20^o C and the maximum temperature was kept for 6 hours, then the same cycle is repeated. During each thermal cycle the thin films resistance is monitored and a draft calibration law is built. The process is stopped only when this preliminary law seemed to be constant with respect to the previous one. During the thermal cycles we recommend to alternatively switch on and off both the thin films and the heater even with different currents. In this way it is possible to reproduce all the typical thermal fields, that will take place inside the probe during the experimental tests.
When the probe thermal curing seems to be finished, it is possible to start the thin films calibration procedure. It is important to have an accurate temperature reference to measure the temperature in the oven and correlate it with an electrical quantity measured by the sensor. We used a thermocouple for this purpose. The thermocouple, connected to the amplifier, is calibrated in a oil bath; it is placed in the oil close to reference temperature Pt 100 sensor. The oil temperature is increased from ambient to 100^oC with steps between 5 and 10 degrees, and monitored with the Pt100 sensor. For each step, when the temperature is stable, the amplifier output tension is measured with a multimeter. Before the measurement, in order to avoid vertical temperature gradients in the oil bath, a magnetic mixer is used. In total 13 points, tensions vs temperature, are taken in the temperature span. For each point, depending on the step amplitude, a

time between 30 and 60 minutes, for the oil bath temperature stabilization, is required. Finally, the calibration law obtained with a best fit interpolation is:

$$T = 97.8330V + 274,043002 \tag{4.1}$$

the R^2 associate at this calibration law is $R^2 = 0,999987$. Figure 4.3 shows the experimental set up, used for the thermocouple calibration. With the calibrated thermocouple

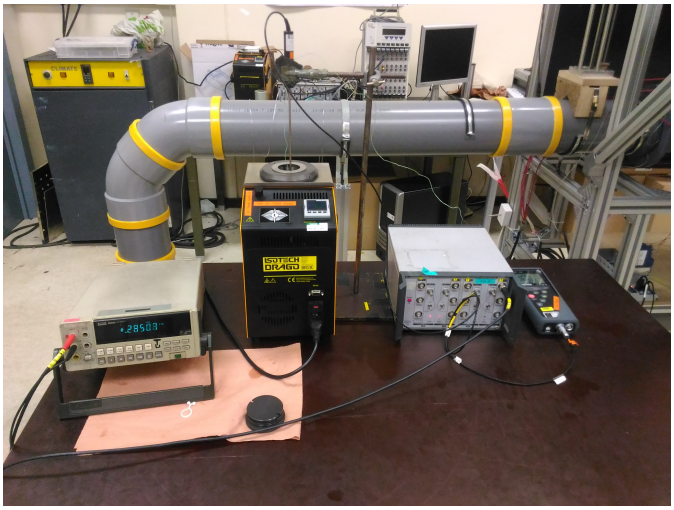

Figure 4.3: Set up for the thermocouple calibration

the thin film calibration is carried out. In the oven we placed thermocouple as close as possible to the thin film probe; we measured the oven temperature with the thermocouple and, at the same temperature, we measured an electrical quantity on the thin film. It is important to consider, during the calibration process, the complete measurement chain used during the tests. In this case it is very difficult: during the real tests the film, connected to the amplification system, is crossed by a constant current and a potential difference is measured. If we want to reproduce this process during the calibration we have to switch on the thin film. Due to the joule effect the thin film temperature will increase and finally the thin film temperature will be different from the temperature measured by the thermocouple. This problem is solved switching off the thin film, during the calibration, and measuring its resistance with a multimeter. The output of the calibration is a temperature versus thin film resistance law. Knowing the thin film constant current we can obtain the final law temperature vs thin film tension. The great disadvantage of this procedure is that it is unable to consider, during the calibration procedure, the influence of thin film supplying and amplification system. The thin film is calibrated starting from ambient temperature until 85 degrees; the temperature steps amplitude is 10^o (5 for the last or first step). Another crucial point of this case is to have stable and equal temperature between the thermocouple and the thin film sensor. In this case, for each temperature step, we waited for 1 hour and half is waited in order to guarantee those conditions. The calibration is repeated several times to check its

stability. It is also important to repeat the calibration procedure before and after the tests campaign; compare the results in order to understand if the tests can influence the law. In figure 4.4 we plot the laws, obtained during the different calibrations.Figure 4.5 presents the errors between the different calibration. The experimental tests in the jet

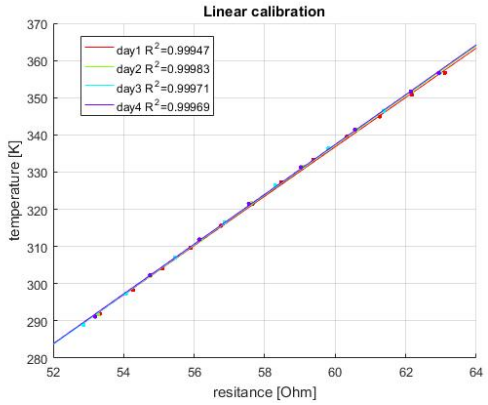

Figure 4.4: Different, linear calibration laws

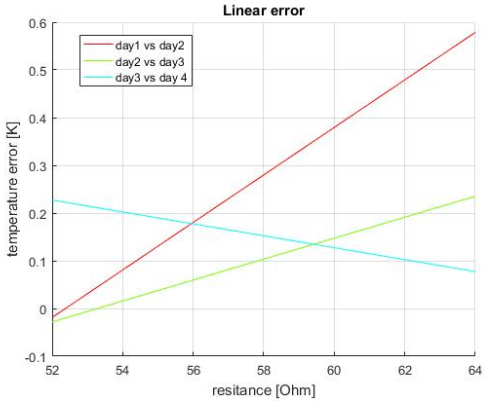

Figure 4.5: Error during different calibration days

are made between calibration 3 and calibration 4. The maximum error between these two laws is 0.2 K. We can conclude that, in this case, the tests don't influence the calibration.
During the calibration we notice a particular non linear thin film behaviour at high temperatures. When the temperature in the oven exceed 60 degrees the curve slope and the R^2 parameter are decreasing. In order to consider this effect we try to interpolate the calibration data with a quadratic polynomial. Figures 4.6 and 4.7 shows the best fit curves and the error between the different days. With respect to the linear case the correlation coefficient is increasing, but the error, between the calibration law in different days remains of the same order. For this reason the simplest, linear solution is chosen. Finally, the selected thin film calibration law is the 3^{th} day linear law:

$$T[K] = 6,69602R[\Omega] - 64.32385 \tag{4.2}$$

4.2 Thin film amplification system

Figure 4.8 contains schema of the thin film control board. Two possible connection types, BNC or RJ45, are available in this case. It is possible to chose 3 different current intensities on the thin film: 5, 10, 15 or 20 mA. When the RJ45 is connected, through an Anderson loop, the thin film is crossed by constant current and the resistance is converted in voltage signal. This signal is amplified by the INA, at 3 possible amplification levels: $\times 1$ $\times 5$ or $\times 10$. Two different operating modes are available the R_0 and the dR . The latter permits to balance the circuit in order to have an initial voltage output equal to

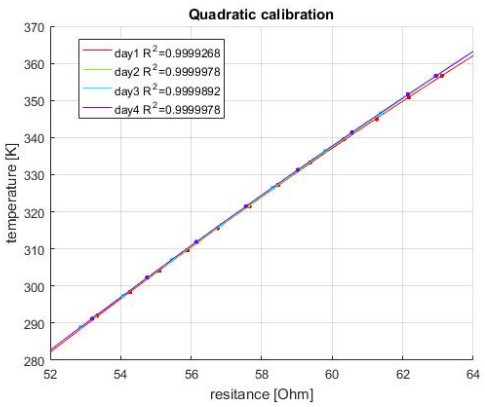

Figure 4.6: Different, quadratic calibration laws

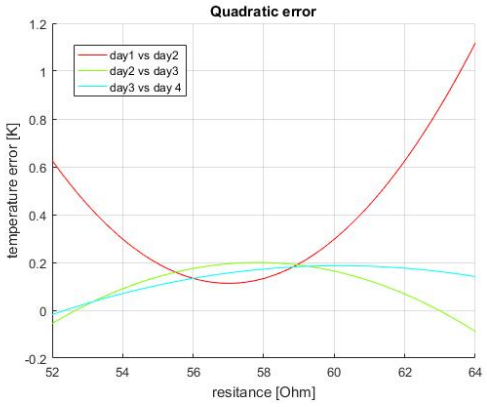

Figure 4.7: error during different calibration days

0 V. In this case, a high frequency response in required so the RJ45 input with an R_0 mode is chosen. The selected thin film current is 5 mA in order to limit the influence of the thin film joule heating that can cause lateral temperature gradient. The INA amplifier is set at 5.
The analytical relation between the wall temperature and the wall heat transfer, in the simplest, one layer case, in the Laplace domain becomes:

$$\overline{T}_w = \frac{\overline{Q}_w(p)}{\sqrt{\rho c k}\sqrt{p}} \tag{4.3}$$

The high frequencies wall temperature fluctuations are dumped a lot, we require an amplification system able to amplified high frequency signal and at the same time reduce the noise amplification. A shaped gain is insert in the system (fig,4.9). A cut off frequency around 200KHz is set to reduce the high frequencies noise. The final outputs of this system are: a raw signal, an HP signal high passed filtered at 60Hz, low passed filtered at 180KHz and amplified $\times 10$ and an LP signal low passed at 500Hz. Figure 4.10 presents an overview of all the gains applied at each channel. The heat transfer box maxiumum voltage output is 12 V, the nominal voltage of the system is 17V and the nominal current is 2A, provided with a dedicated power supply. The heat transfer box calibration and the amplification routines are provided by C. Sciamanna [32].

The available acquisition system is a NICOLET genesys. Seven boards are available with eight channels each one. The sample resolution is 16 bit. During the experimental tests all the 3 channels are sampled. The LP channel is sampled at 20KHz for 10 second; the RAW and the HP channels are acquired at 500KHz only for 3 s in order to limit the output files dimension.

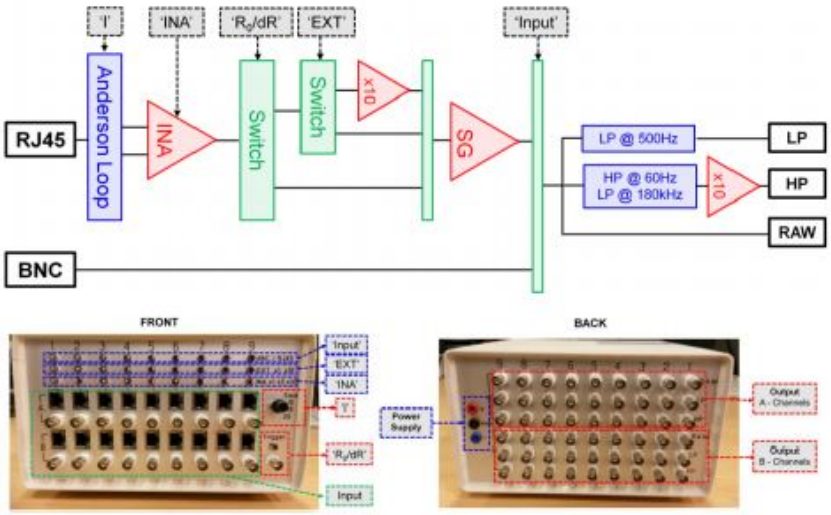

Figure 4.8: Schematic representation of the heat transfer control box

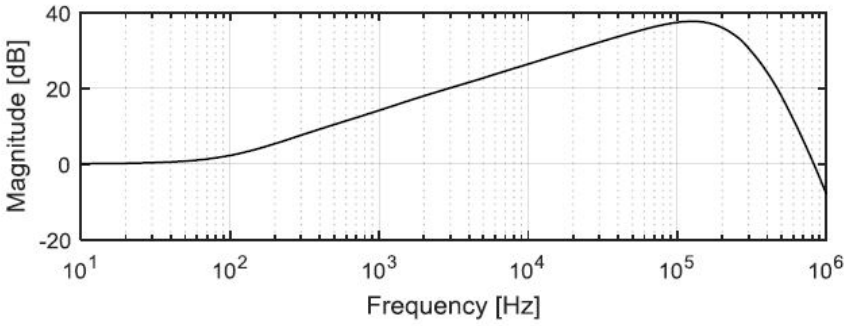

Figure 4.9: Shaped gain

4.3 Experimental set up

The first point is to reproduce with a simple set up the CT3 transient operating conditions. A hot air jet is created with a 15mm of diameter nozzle. The pressurized air supply is connected to a heater able to warm up the flow. Upstream the nozzle a settling chamber is positioned and the flow total temperature is measured by the calibrated thermocouple and the dynamic pressure is known using a total pressure probe connected with a Validyne transducer. In order to reproduce the transient conditions a fast opening shutter, controlled with a pneumatic actuator is positioned just in front of the jet. The probe is positioned just behind the shutter. Figure 4.11 presents a general schema of this set up. The thin film is connected to the RJ45 port of the heat transfer box and the probe heater is connected to a power supply. The current and the tension at the heater

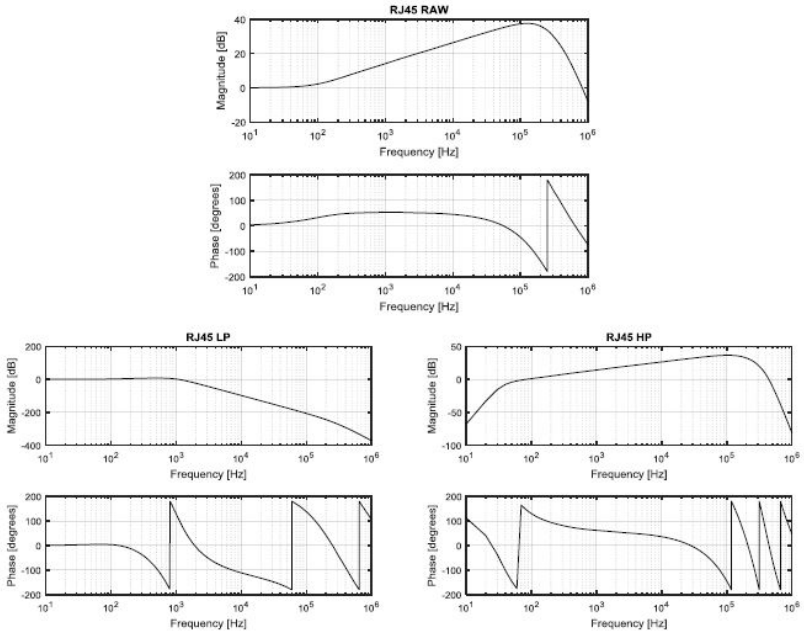

Figure 4.10: Final transfer function for each output channel

are measured with two multimeters in order to know exactly the electrical power. Before the test begins the shutter is closed in front of the jet, the pressure transducer measures a high pressure due to the losses present between the jet exiting and the shutter. When the test begin the shutter is opened; the thermocouple, the validyne and the LP thin film signals are sampled for 10 second at 20KHz. The RAW and HP channels are acquired at 500KHz for 3 seconds. Figure 4.12 contains a photo representing the used set up.

4.4 Preliminary test

Some preliminary tests are carried out in order to understand the heater power and the time required to reach the probe thermal equilibrium condition at different wall temperatures. The first point is to estimate the natural convection h coefficient. The Rayleigh number is:

$$Ra_D = \frac{g\beta\Delta T D^3}{\nu\alpha} = 550 \tag{4.4}$$

The considered ΔT is the temperature difference between the probe wall and the fluid, as first approximation, is 50 K. Using the Ra_D it is possible to estimate the mean Nusselt number on the cylinder surface[18].

$$\overline{Nu}_D = \frac{2}{log(1 + 5.01/Ra^{0.26})} \tag{4.5}$$

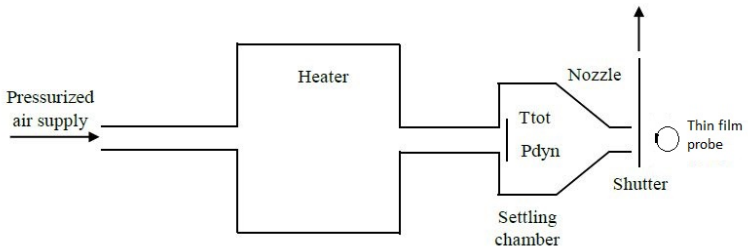

Figure 4.11: Schema of the experimental set up

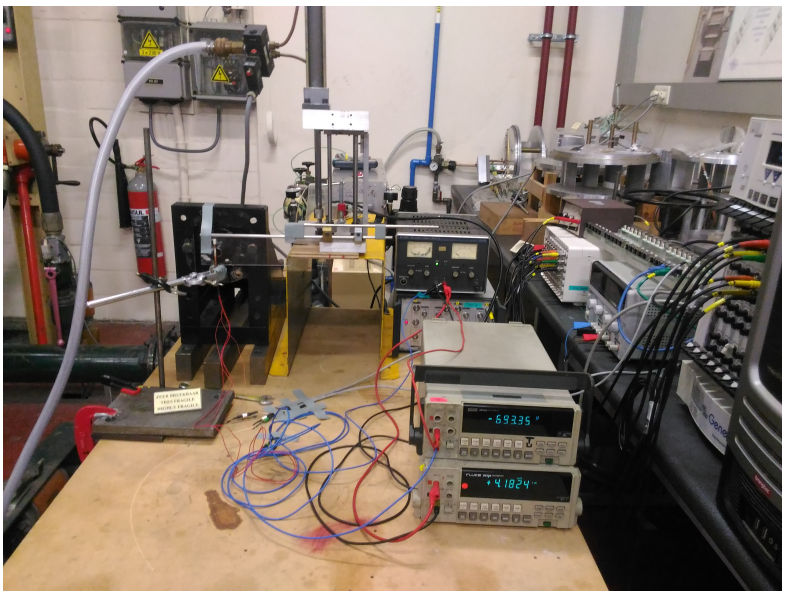

Figure 4.12: Experimental set up

Finally the mean h is founded:

$$\overline{h} = \frac{\overline{Nu}k}{D} = 16.5\frac{W}{m^2K} \tag{4.6}$$

Knowing h and modelling the probe as a first order thermal system; it is possible to estimate the time required to reach the thermal equilibrium. The constant time of the system, neglecting the KAPTON layer, is:

$$\tau = \frac{mc_p}{hS} = \frac{D}{4}\frac{\rho c_p}{h} = 143s \tag{4.7}$$

to reach the probe thermal equilibrium it is necessary to wait some minutes.
Knowing the heater resistance (almost 6 Ω depending from the substrate temperature) it is possible to calculate the heater voltage required to reach a fixed temperature on the

wall. Writing the probe thermal equilibrium we obtain:

$$T_{wall} = T_{amb} + \frac{V^2}{RL_{heater}\pi D_{probe}h} \tag{4.8}$$

Some probe tests are made in order to validate this draft law. Figure 4.13 presents the results . The theoretical model over estimates the temperature that is possible to reach with a given heater ΔV. This is due to the difficult h coefficient estimation and to the effects of the lateral conduction for our low aspect ratio cylindrical probe. The error increases with the probe temperature; when the temperature grows up the resistance increases and, at constant voltage, the heater power is decreases.

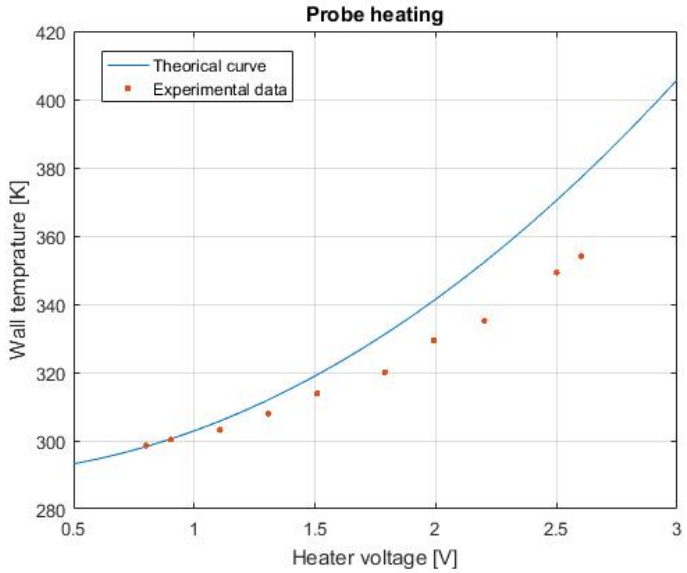

Figure 4.13: Effect of the probe heating on the temperature surface

4.5 Experimental results

During the test procedure the jet Mach number is fixed at 0.3. The flow is warmed up at a total temperature of almost 313 K; it is difficult to regulate the heater power in order to maintain the jet temperature constant, during the tests a change in jet temperature of almost 2 degrees is detected . The probe is heated at different levels with its heater, starting form ambient temperature and arriving at 350 K. At the beginning the shutter is closed and the probe, just behind, is in thermal equilibrium with the ambient. When the shutter is opened the pressure can discharge in the external ambient, the pressure measured by the valydine transducer decreases and the probe is cooled or warmed by the flow. The wall temperature, thermocouple temperature, and valydine pressure are acquired with the genesis.

The first step of the post process procedure is to filter the signal in order to reduce the noise. In this constant temperature case, only the LP signal is used from the thin film. A Butterworth 3th order filter with a cutting frequency of 50 Hz is applied to the thermocouple, valydine and LP signals. Later, the synchronization of the signals coming from the different tests is necessary. The pressure signals time derivatives are computed; the synchronization is made using the time when this value reach the minimum. Figures 4.14 and 4.15 shows the synchronized signals of total pressure and flow total temperature. For the pressure signals the ambient pressure is added in order to have, during the test, the flow total pressure. Figure 4.16 contains the wall temperature time histories,

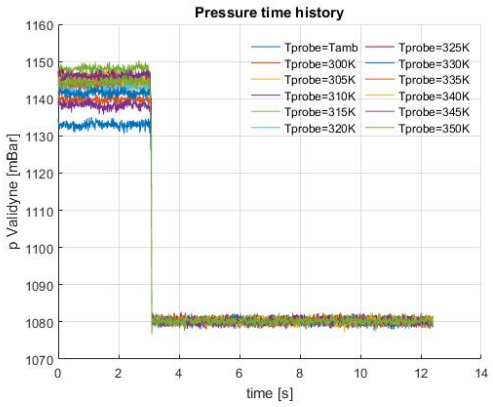

Figure 4.14: Total pressure signals

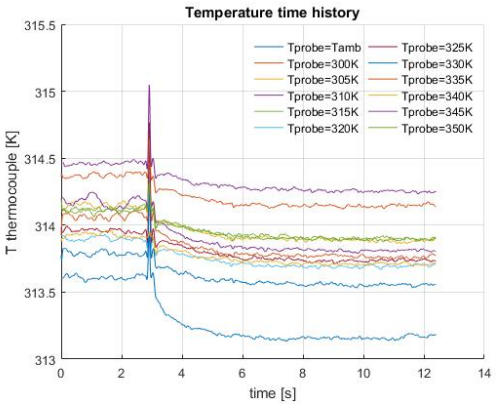

Figure 4.15: Total temperature signals

obtained by knowing the thin film tensions, the thin film currents and the calibration law, resistance versus temperature. During the test it is difficult to set exactly the probe

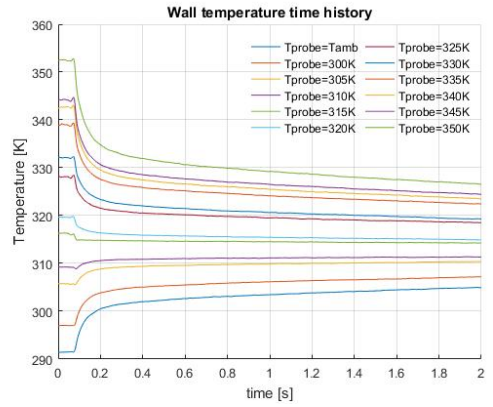

Figure 4.16: Filtered LP wall temperature signals

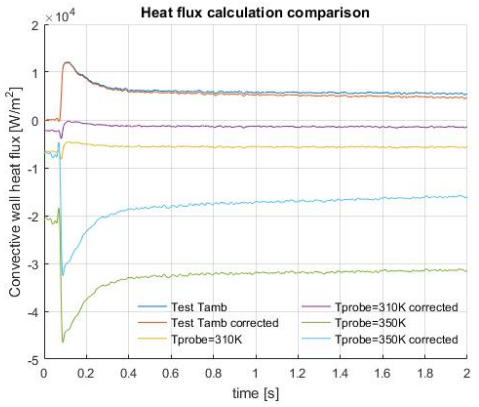

Figure 4.17: Comparison between heat flux computed with different models

temperature, just a draft regulation is made. The total flow temperature during the tests is maintained between 313.2 and 314.2 degrees. For initial probe temperatures higher than 313 K the flow is cooling the probe; for initial temperatures lower than 313 K the flow is warming the probe. Using a 1D Comsol model very similar to the model used in the chapter 3 the conductive heat fluxes are computed. The initial steady solution is found imposing the heater heat flux on the right of the domain and the first sampled temperature on the other side. Later, the wall time history is imposed and the wall heat flux is computed. Both, the simple 1D and the axialsymmetrical models are tested. figure 4.17 shows the models output at some probe temperatures(positive heat flux is entering in the probe). If the heater is switched off the output of the two models is very similar. When the heater power increases the simple 1D model starts to over estimate the heat flux at wall. The normal model considers, in the steady state conditions, the same heat flux on the heater and on the probe wall. The heater surface is smaller than the probe external surface so the steady state heat flux for area unit has to be lower on the probe surface. The corrected symmetrical model is able to consider this effect. It is necessary to consider the electrical heat flux given by the thin film. Subtracting the electrical heat flux from the conductive one the convective heat flux is found. Figure 4.18 shows the convective heat flux time histories computed with the 1D corrected model, for all the considered probe temperatures. When the convective heat fluxes are available, it

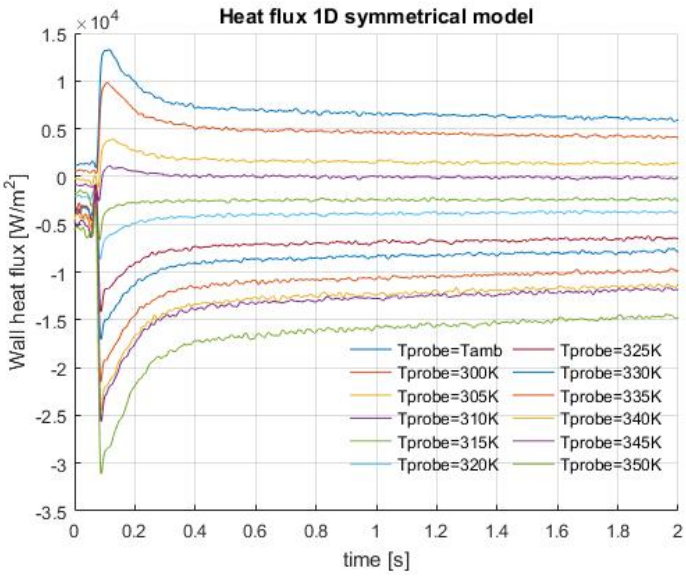

Figure 4.18: Convective heat flux time histories computed with the corrected model

is possible to proceed with the linear interpolation. 12 time histories of wall temperature and wall heat flux are available so at each time step a best fit, linear interpolation can be done.Figure 4.19 contains an example of the linear interpolation at some time steps . The interpolation process is repeated using the wall heat fluxes computed with both the 1D models. Figure 4.20 shows the R^2 coefficient time histories useful to estimate

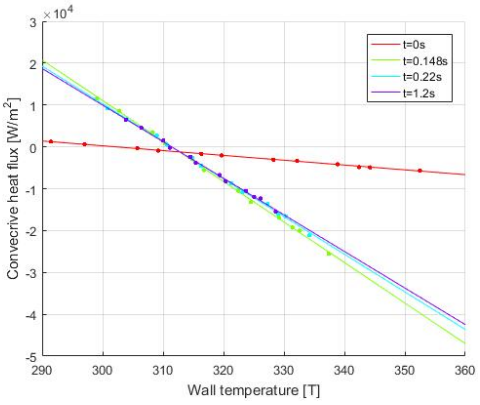

Figure 4.19: Example of the best fit line at some time instant using the corrected heat flux model

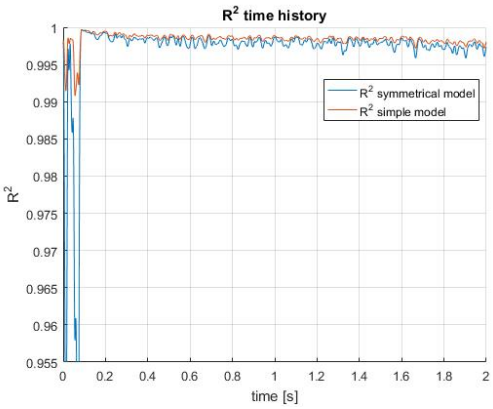

Figure 4.20: R^2 time history

the quality of the interpolation. When the shutter is closed it is difficult to reproduce the flow during the different tests, so the R^2 coefficient is quite low. When the shutter is open the correlation increases a lot and at the test begins an R^2 value of 0.999 is detected. Then, probably due to some later conduction effect, the correlation decreases a bit but R^2 remains around 0.997 for all the test duration. The very high R^2 coefficient

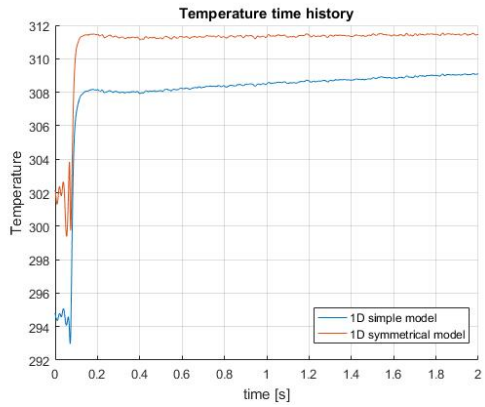

Figure 4.21: Temperature time history

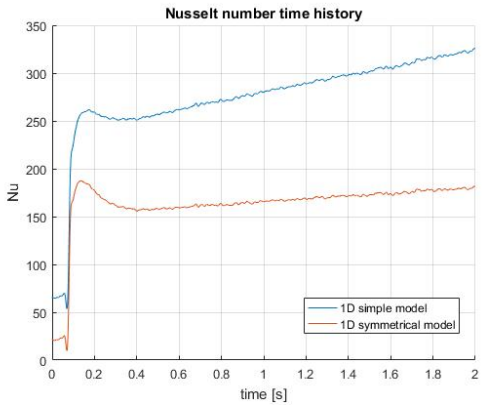

Figure 4.22: Nusselt time history

confirms ability to reproduce the same kind of flow during the different tests and the high linearity in the heat flux phenomena for wall temperature in a range of 60 K. Using the linear interpolation it is possible to compute the total temperature and the Nusselt number time histories. Figures 4.21 and 4.22 contains these trends computed using the heat flux coming from both the models. When the shutter is open, the measured

temperature, using the corrected model, reaches 311.6 K. This measure remains very stable during the test time. The error with respect to the mean temperature measured with the thermocouple upstream the jet, is almost 2.5K; whereas using the normal bar model the error increases. This error could be caused by the distance between the nozzle and the probe. In order to insert the shutter, avoiding all kind of mechanical influences, the probe is positioned at a distance of almost 30 mm from the nozzle. This is a limit position for the jet potential core there could be some influences from cold ambient. Another problem could be the flow temperature decreasing during the expansion in the metal nozzle with no insulating layer. Seeking the problem in the measurement chain, an improved thin film calibration procedure, able to consider also the cable and the heat transfer box influence, needs to be developed. Another idea is to sample, with genesis channels, the current and the voltage at the probe heater during the tests; in this way a more accurate boundary conditions at the 1D model border could be fixed. Moreover the Nusselt number time history is coherent with the expected values. At the test beginning there is only the natural convection so the Nu is low. When the shutter is open the velocity near the probe increases a lot and also the convection is increasing. There is an overshoot because there is compressed air in the nozzle and in the settling chamber; when the shutter is open this high pressure is discharged in the ambient and creates high velocity and high convection on the probe surface. Later, the flow reaches a regime. During the test the Nusselt number increases with constant slope, this effect is not real but we believe it is due to some lateral conduction effect that we are not able to estimate with our 1D model. Using the 1D corrected model this effect decreases a lot. The computed Nusselt is consistent with the CFD calculations carried out in chapter 2. According to the CFD model the mean Nusselt on the sensor is 115 or 210 for TU of 0.2% or 5% respectively. In this case the level of turbulence could have a value between this two values and the Nusselt number is between 160 and 180. Processing data using the normal 1D model, the Nusselt number is over estimated.
Finally, figure 4.23 contains a complete schema of the experimental and post process procedure.

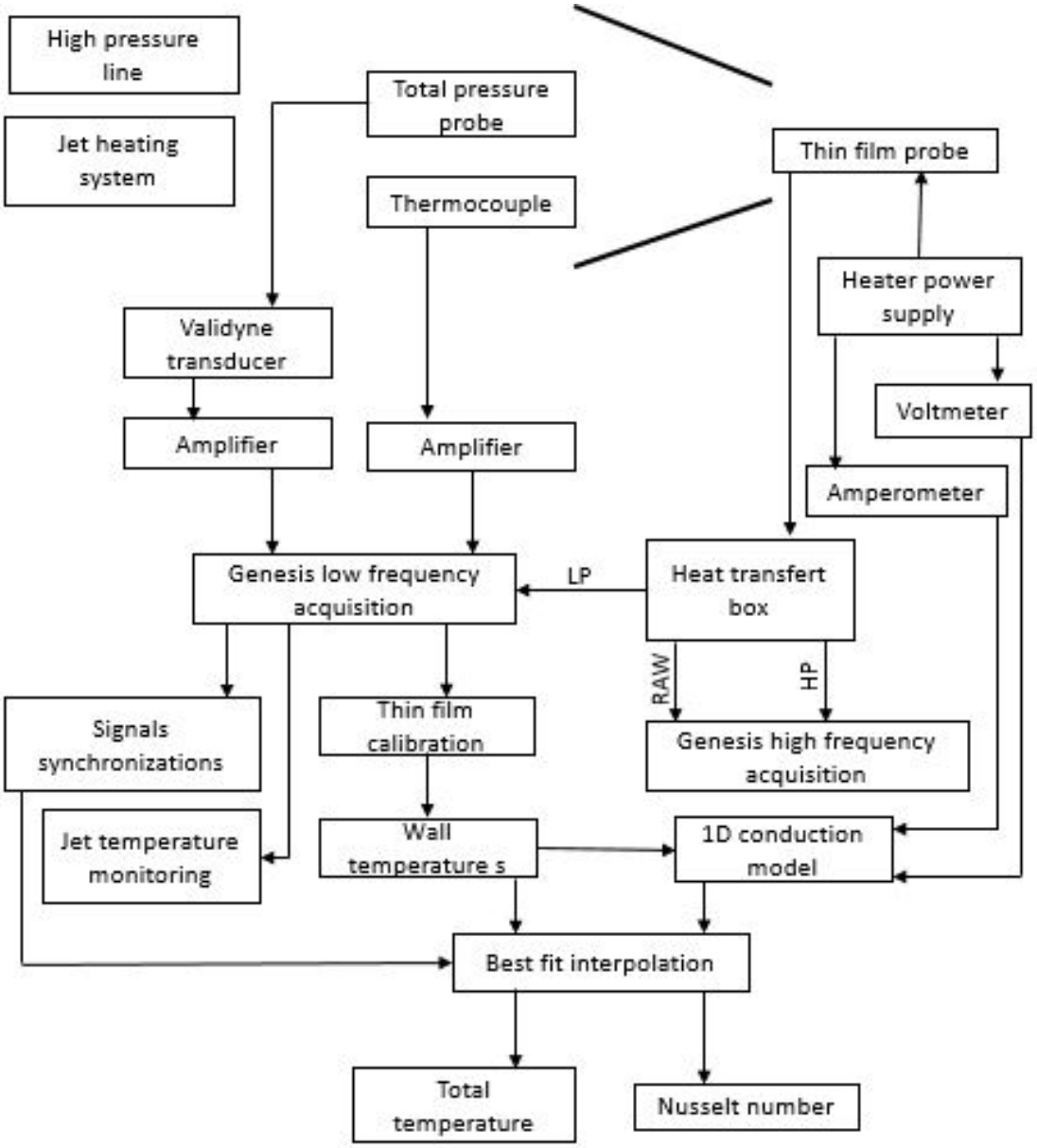

Figure 4.23: Experimental set up and post processing

Conclusions

We made the preliminary design of a new concept single thin film probe. The final probe needs to work in the CT3 transient VKI facility and measure the temperature fluctuations with a frequency response of 25KHz or more. The final selected solution presents 11 thin films equally distributed along the span of 5 mm diameter cylinder. A heater is positioned in the probe and is used to reach different probe initial temperatures. The thin films are used for the wall temperature monitoring. The wall temperature time histories are fixed as a input of a 1D conduction model useful for the wall heat flux calculation. Finally, using a best fit interpolation the flow total temperature can be derived.
A numerical 2D model is built, validated and computed in order to detect the probe fluid dynamics behaviour. The error made by the probe is estimated and it seems bounded to an acceptable range. Simulations with different heat flux wall conditions are launched in order to estimate the Nusselt number around the cylindrical probe and for detecting the non linearities in the heat transfer phenomena. The results for both Nusselt number and non linear analysis, are really consistent with data coming from the literature.
Starting from some theoretical thermal consideration a first geometry for the probe is produced. Using data coming from the CFD calculations a 2D thermal model of the probe is built and solved with Comsol. With this model the post process routine is developed and numerically tested. A 3D model is built and solved in order to understand if the 3D effects can influence the temperature measurement, fortunately we detect very little influence. The same analysis are repeated for the double layer configuration. Finally some thin film design criteria are analysed.
A probe prototype is built using the double layer configuration. The curing and calibration procedure is designed and performed. It is not simple to obtain a stable calibration condition. Another problem in the built prototype is the low mechanical resistance in the double layer gluing. During the curing and test processes, in the posterior part, the KAPTON layer starts to unglue from the MACOR substrate. Some transient tests in constant temperature jet are carried out. The heat flux linearity is validated with very good accuracy. The flow temperature estimation is affected by an error of almost 2K. This could be caused by a set up, unable to measure the reference temperature in the exact probe position. Another error source is the difficulty in the complete thin film probe measurement chain calibration.

Future developments

An additional work is required with the built prototype. A new calibration procedure able to take into account the complete measurement chain needs to be developed. Another point will be to test the probe in different temperature jet flows. Furthermore it would be interesting to make some measurement in an ambient temperature jet. In this case, it is impossible to have heat flux measurements at wall temperature lower than the jet temperature but, using the detected linearity in the heat flux phenomena, it will be possible to understand if the error, in the temperature measurement, comes from the influence of the ambient temperature. Other possible tests will consider different thin film currents, in order to understand the influence of the lateral temperature gradient created by the thin film. The probe validation will continue with the experimental measurement of the error due to the sensor misalignment with the flow, in order to validate the CFD results presented in chapter 2. Finally, the idea is to create some high frequency temperature fluctuations and test the probe dynamic response. A suggested improvement in the measurement chain consists in the acquisitions, using 2 low sampling frequency genesis channels, of the voltage and the current on the heater. With this solution we will have more accurate estimation of the heater power, useful for imposing the heat flux condition in the 1D model.
Another goal will be to finalize the design, using all the numerical calculations and the experimental experience to obtain the final probe technical drawings. This phase has also to take into account the single layer, more robust solution. An important point is to improve the heater design. The actual probe heater has a high sensitivity to the substrate temperature. During the tests it is difficult to reach a stable temperature field in the probe, because when its temperature increases the heater resistance increases to. At the same voltage power supply, if the resistance increase the power decrease causing a decrement in the probe temperature.
Finally, a complete post process routine able to manage automatically all the experimental data is required. In particular, it is necessary to develop a free and fast 1D code, able to implement also the symmetrical correction. The code will be able to post process temperature time histories, sampled at very high frequency (500 kHz or 1MHz), for a sampling time of almost 1 second.

Bibliography

[1] Arenz M. C. , Weigel B. , Habermann J. , Staudacher S., Rose M. G., Berns W., Lutum E. *Development and Application of a Fast-Response Total Temperature Probe for Turbomachinery*

[2] Bergman T. L., Lavine A. S., Incropera F. P., Dewitt D. P. table 7.7 *Fundamental of heat and mass transfer*

[3] Bonetti G.(2013), *Evaluation of miniaturized fast response probes*

[4] Bruun H. H. *Hot wire anemometry* 1995

[5] Buttsworth B. R. , Jones T. V. *A fast response high spatial resolution total temperature probe using a pulsed heating technique.*

[6] Buttsworth B. R. , Jones T. V., Chana K. S. *Unsteady total temperature measurements downstream of a hight pressure turbine*

[7] Carvalho A. J. (2013), *Development and characterization of fast-response probes for thermal measurements in high-speed turbo machinery*

[8] Clark J. P., Grover E. A. (2006) *Assessing convergence in predictions of periodic-unsteady flow fields*

[9] Doorly J. E., Oldfield M. *The theory of advanced multi-layer thin film heat transfer gauges* 1987

[10] Fey U. ,König M. ,Eckelmann H. (2016) *A new Strouhal-Reynolds-number relationship for the circular cylinder in the range* $47 < Re < 2 \cdot 10^5$

[11] *Fluent theory guide* version 16.2

[12] *Fluent manual user online version*
https : *//www.sharcnet.ca/Software/Fluent*6*/html/ug/node*256*.htm*

[13] Green B. R. (1996) *3-D unsteady simulation of a modern high pressure turbine stage*

[14] Goldstein R. J., Boyong H. (2001) *Energy Separation and Acoustic Interaction in Flow Across a Circular Cylinder*

[15] Hogendoorn C. J. ,De Lange H. C. , Van Steenhoven A. A. *Design optimization for fast heat-transfer gauges* 1997

[16] Korobkin I.,Gruenewald K. H.(1950) *Investigation of Local Laminar Heat Transfer on a Hemisphere for Supersonic Mach Numbers at Low Rates of Heat Flux*

[17] Kulyakhtin A., Shipilova O.,Muskulus M.(2014) *Numerical simulation of droplet impingement and flow around a cylinder using RANS and LES models*

[18] Kyte J. R., Madden A. J., Piret E. L. *Natural-convection heat transfer at reduced pressure* 1953

[19] Lavagnoli S., Maesschalck C. D., Paniagua G. (2010) *Analysis of the Heat Transfer Driving Parameters in Tight Rotor Blade Tip Clearances*

[20] Lienhard J. H. (1966), *Symposium of Lift, Drag, and vortex frequency data for rigid circular cylinder*, Technical extension service.

[21] Lowery C. W. ,Vachon R. I. (2016) *The effect of turbulence on heat transfer fro heated cylinders*

[22] (2009) Mansour M. , Chokani N. , Kalfas A. I., Abhari R. S. *Unsteady Entropy Measurements in a High-Speed Radial Compressor*

[23] (2008) Mansour M., Kalfas A. I., Abhari R. S., Chokani N. *Unsteady Entropy Measurements in a High-Speed Radial Compressor*

[24] Van Meel D. A. (1962) *A method for the determination of local convective heat form a cylinder placed normal to air stream*

[25] Merrick R., Bitsuaml G. (1950) *Control of flow around a circular cylinder by the use of surface roughness: A computational and experimental approach*

[26] Rodriguez O.(1984) *The Circular Cylinder in subsonic and transonic flow*

[27] Roshko A.(1950), *Experiments of flow around circular cylinder at very high reynolds number*

[28] Salazar A.(2006) *Energy propagation of thermal waves*

[29] Sanitjai S.,Goldstein R. J. (2004) *Forced convection heat transfer from a circular cylinder in cross flow to air and liquids*

[30] Schmidt E., Wenner K. (1941) *Warmeabgabe uber den Umfang eines angeblasenen*

[31] Schultz D. L. ,Jones T. V. (1973) University of Oxford *Heat-transfer measurements in short duration hypersonic facilities*

[32] Sciamanna C. ,Lavagnoli S., Cernat B. *Calibration and data reduction of heat transfer measurement for transient turbomachinery testing* 2017

[33] Shao J. ,Zhang C.(2006) *Numerical analysis of the flow around a circular cylinder using RANS and LES*

[34] Shyam V. , Ameri A., Luk D. F. , Chen J. P. *3-D unsteady simulation of a modern high pressure turbine stage using phase lag periodicity: analysis of flow and heat transfer*

[35] Ulbricht I. *The double thin film probe for high frequency temperature measurements*

[36] Vaz G. ,Mabilat C. , Van der Wal R. , Gallagher P.(2007) *Viscous flow computations on smooth cylinders: a detailed numerical study with validation*

[37] White F. M. (1950) *Viscous Fluid Flow* McGraw-Hill pag 522

[38] Zhenhua X.,Zuoli X.,Yipeng S. and Shiyi C. (2016) *Mach Number Effect of Compressible Flow Around a Circular Cylinder*